Review

Victor Charles*, Ebuka Ikegwuonu P., Ndepana A. Gaya

Solid-Solutions as Supports and Robust Photocatalysts and Electrocatalysts: A Review

https://doi.org/10.1515/cse-2020-0002
received August 9, 2019; accepted December 20, 2019.

Abstract: Some solid solutions have been strongly utilized over the years as good materials for the synthesis of electrocatalysts and photoctalysts. Sometimes, they are used as supports in order to improve electrocatalytic and photocatalytic properties. We show various achievements of solid solutions as good electrocatalysts, and also, good electrocatalysts support materials in oxygen reduction reaction (ORR), hydrogen evolution reaction (HER) and oxygen evolution reaction (OER). Also, we demonstrate various works utilizing solid solutions as good photocatalysts, and good photocatalysts support materials in overall water splitting and carbon dioxide reduction. In all these reports, solid solutions proved to posses the necessary properties needed of any material as electrocatalysts and photocatalysts. In many cases, their use as catalysts supports recorded great improvements. X-ray photoelectron spectroscopy (XPS) was largely used to confirm the chemical environment of the results obtained, together with X-ray diffraction (XRD). In the electrochemical methods, cyclic voltammograms (CVA), chronoamperometry and rotating disk electrode (RDE), were also carried out. Linear sweep voltametry (LSV) curve was carried out in some cases to measure the current at a working electrode, and tables were shown for clear explanation. In addition, a photoluminescence spectrum (PL) was used to probe the electronic structure of the various solid solutions.

***Corresponding author: Victor Charles,** Department of Chemistry, Modibbo Adama University of Technology, Yola, Nigeria, E-mail: victorcharles2020@mails.ucas.ac.cn
Ebuka Ikegwuonu P., Chemistry Department, Faculty of Science, University of Alberta, Canada
Ndepana A. Gaya, Institute of Chemistry, University of Chinese Academy of Sciences, Beijing, China

Keywords: Solid-solution; overpotential; electrocatalysis; photocatalysis.

1 Introduction

Solid Solution is a crystal containing a second constituent which fits into and is distributed in the lattice of the host crystal. They always consist of two or more types of atoms or molecules that share a crystal lattice – such as metal alloys. Most steels used in construction are also solid solutions of iron and carbon. The ability of the carbon atoms to efficiently fit within the crystal lattice of the iron adds strength to its structure. Some examples of solid solutions include gallium arsenide (GaAs) with gallium phosphide (GaP), aluminum arsenide (AlAs), or indium arsenide (InAs) and many more. The choice of constituent solids depends on the desired properties of the solid solution to be obtained.

Solid solutions have found applications in different fields some of which include its use as electrocatalysts, photocatalysts having high activity, high selectivity and high stability, as well as catalyst supports. A study of experimental and theoretical studies carried out by Lashkarev et al. reveals that solid solution materials based on a wide, direct bandgap, zinc oxide semiconductor is promising for the development of a new generation of devices to be used in optoelectronics, photovoltaics and nanoplasmonics [1]. Some chemists used solid solutions to improve electrocatalytic properties of catalysts in order to obtain good electrocatalytic performance which include; high activity, high selectivity high stability and low overpotential [2]. Wen et al. showed this when they used solid solutions (Zr, Ce)O_2 to improve the electrocatalytic properties of Pd-based catalyst for the direct fuel cells. They determined that "the inclusion of solid solutions (Zr, Ce)O_2 as the supporting material can greatly enhance the activity and also, the anti-CO- poisoning Pd/C catalyst for ethylene glycol electro-oxidation in KOH medium." First

principle calculation reveals that the improved activity and anti-CO-poisoning of the electrocatalyst resulted from the Pd cluster found on the surface of the (Zr, Co)O_2 solid solution which led to weaker Pd-C bonding and smaller CO desorption driving force. Studies have shown that solid solutions have been used as supports or materials to synthesize catalysts possessing qualitative features of high selectivity, high activity and low overpotential. Its application extends to the reduction of carbon dioxide.

Photocatalysis and electrocatalysis are used in various applications such as oxygen reduction reaction (ORR), oxygen evolution reaction (OER), hydrogen evolution reaction (HER), overall water splitting, carbon dioxide reduction and so on. In all these reactions, a lot of interest has been drawn to the use of solid solutions as supports or catalysts that show outstanding electrocatalytic and photocatalytic performance. The technologies are environmentally friendly: use of water splitting to obtain hydrogen for energy generation, and electrocatalysis of carbon dioxide reduction. In electrocatalysis and photocatalysis, different solid solutions have been used by different chemists as supports and also as desired electrocatalysts and photocatalysts which have satisfied the expected requirements. Many researchers have reviewed various works carried out by different chemists on the use of solid solutions as photocatalysts with outstanding performance or as catalyst supports. However, no review has been carried out which comprehensively highlights various works carried out by chemists on the use of solid solutions as electrocatalysts for oxygen evolution reaction (OER), hydrogen evolution reaction (HER), oxygen reduction reaction, and photocatalysts for overall water splitting and carbon dioxide reduction with improved performance or as catalyst supports in electrocatalysis and photocatalysis.

Herein, we give a comprehensive review which shows recent developments on progresses made by different researchers on electrocatalysis and photocatalysis, involving the use of solid solutions as electrocatalysts and photocatalysts with improved performance or as catalyst supports. We comprehensively give some advances in electrochemical catalysis, oxygen reduction reaction, oxygen evolution reaction, hydrogen evolution reaction, overall water splitting and photocatalysis of carbondioxide reduction. Various electrochemical methods and characterizations which revealed more information and confirmed the outstanding performances of the various synthesized electrocatalysts and photocatalysts were also demonstrated.

1.1 Advances in Electrocatalysis

Electrocatalysis is a catalytic process involving oxidation and reduction reactions through the direct transfer of electrons, which requires electrocatalysts to lower the overpotential of the reactions [1]. It does so by facilitating the conversion between electrical and chemical energy in fuel cells and electrolysis technologies [2]. The sole aim of electrocatalysis is to increase the electrochemical reaction rates taking place at the surface of electrodes [3]. Recently, solid solution nanoparticles were discovered as good electrocatalysts for variety of reactions, such as in fuel cells, oxygen evolution reaction, hydrogen evolution reaction, carbon dioxide reduction, overall water splitting and many more [4]. However, the mechanism of the electrochemical reaction depends on the electrocatalysis taking place, as different electrocatalytic technologies have different mechanism. In all of these various electrocatalysis, the effect of solid solutions either as catalyst or catalyst support has been remarkable. Lin and his colleagues studied the chromium-ruthenium oxide solid solution electrocatalyst for highly efficient oxygen evolution reaction in acidic media [3]. They reported an iridium-free and low ruthenium-content oxide material ($Cr_{0.6}Ru_{0.4}O_2$) derived from a metal-organic framework with remarkable oxygen evolution reaction performance in acidic condition. Ellis and his Co-workers also, through a study on Anion-Induced Solid Solution Electrochemical Behavior in Iron Tavorite Phosphates, reported the synthesis of a mixed hydroxy-fluoro iron tavorite, $LiFePO_4(OH)_{0.4}F_{0.6}$ which demonstrated solid solution behavior on electrochemical cycling in a Li-ion cell [4]. The work revealed a mixed hydroxyfluorophosphate, $LiFePO_4(OH)_{0.4}F_{0.6}$, which demonstrates solid-solution behavior in an electrochemical cell over the entire lithium compositional range $Li1+xFePO_4(OH)_{0.4}F_{0.6}$, at an average potential of 2.6 V vs Li. In the same vein, Ghadge, Shrinath Dattatray, et al, studied fluorine substituted (Mn,Ir) O_2:F high performance solid solution oxygen evolution reaction electrocatalysts for PEM water electrolysis [5]. They identified a reduced noble metal content, fluorine doped, solid solution of MnO_2 and IrO_2, denoted as $(Mn_{1-}xIrx)O_2$:F (x = 0.2, 0.3, 0.4), OER electrocatalyst system exhibiting lower overpotential and higher current density than the state of the art IrO_2 and other previously reported systems for PEM water electrolysis . Their report demonstrates remarkable ~60–80% reduction in noble metal content along with lower overpotential and excellent electrochemical performance clearly demonstrating the potential of the $(Mn_{1-}xIrx)O_2$:F system as an OER electro-catalyst for PEM water electrolysis.

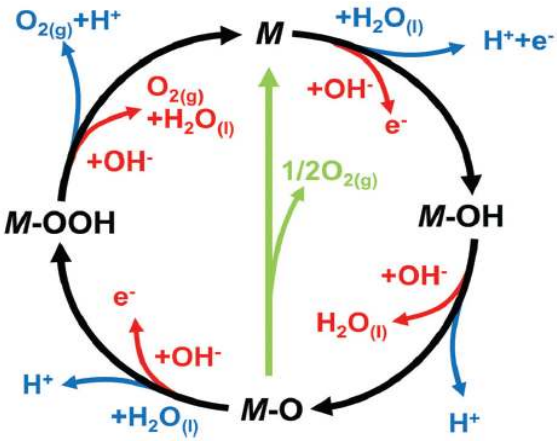

Figure 1: The OER mechanism for acid (blue line) and alkaline (red line) conditions. The black line indicates that the oxygen evolution involves the formation of a peroxide (M–OOH) intermediate (black line) while another route for direct reaction of two adjacent oxo (M–O) intermediates (green) to produce oxygen is possible as well. Adapted from Royal society of chemistry, *Chem. Soc. Rev., 2017, 46, 337*

Kibis et al. studied the redox properties of solid solution $Rh_xCe_{1-x}O_{2-\delta}$ in correlation with its catalytic activity in CO oxidation [6]. They synthesized Rh/CeO_2 catalysts using the coprecipitation method. Their work revealed the formation of homogeneous solid solutions ($Rh_xCe_{1-x}O_{2-\delta}$) with a high degree of defects and microstrains in the fluorite lattice of CeO_2.

2 Oxygen Evolution reaction

This is the complementary anodic, half reaction in electrochemical water splitting. Requiring four proton and electron transfers per oxygen molecule, the OER is the more complex of the two half reactions and is, consequently, responsible for the majority of inefficiency in electrolyzer devices. In acidic media, only Ir-based catalysts have shown high activity and stability for the OER. In alkaline media, catalyst material restrictions are relaxed and many first-row transition metal oxides show high activity for the OER.

2.1 Basic Mechanistic Principles of oxygen evolution reaction (OER)

Oxygen evolution reaction is the half reaction of the water splitting reaction which takes place at the cathode [7]. It generates oxygen gas through several electron/proton complex reaction pathways as shown in figure 1. It also consists of four elementary steps, and, therefore, strongly depends on the pH of the electrolyte. In the acidic pH, the reaction proceeds through the oxidation of two water molecules producing single oxygen molecules having four proton-coupled electron transfer steps. In the alkaline pH, the hydroxyl group is converted into oxygen and H_2O molecules by way of four electron transfer steps. OER in acidic pH and alkaline pH are summarized as follows;

$$H_2O + * \rightleftarrows OH^* + (H^+ + e^-) \quad (1)$$

$$\Delta G_1 = \Delta G_{OH^*} - \Delta G_{H2O} - eU + KTln\,[H^+]$$

$$OH^* \rightleftarrows O^* + (H^+ + e^-) \quad (2)$$

$$\Delta G_2 = \Delta G_{0^*} - eU + KTln\,[H^+]$$

$$O^* + H_2O \rightleftarrows OOH^* + (H^+ + e^-) \quad (3)$$

$$\Delta G_3 = \Delta G_{OOH^*} - \Delta G_{O^*} - eU + KTln\,[H^+]$$

$$OOH^* \rightleftarrows * + O_2 + (H^+ + e^-) \quad (4)$$

$$\Delta G_4 = \Delta G_{O2} - \Delta G_{OOH^*} - eU + KTln\,[H^+]$$

The proposed reactioan mechanism for OER in basic conditions

$$OH^- + * \rightleftarrows OH^* + e^- \quad (5)$$

$$OH^* + OH^- \rightleftarrows O^* + H_2O + e^- \quad (6)$$

$$O^* + OH^- \rightleftarrows OOH^* + e^- \quad (7)$$

$$OOH^* + OH^- \rightleftarrows * + O_2 + H_2O + e^- \quad (8)$$

Where * represents active site of catalyst, and OH*, O*, and OOH* represents the adsorbed intermediate species which are the same in both acidic and basic pH. Thus, the free energy changes during OER in both acidic and basic solutions are calculated by the same equations (Equations (1)–(4)). The OER η (ηOER) is measured as the difference of the maximum value among ΔG1 through ΔG4 and the equilibrium potential (1.23 V), shown in the following equation.

$$\eta^{OER} = max\,(\Delta G_1, \Delta G_2, \Delta G_3, \Delta G_4) / e - 1.23\ V \quad (9)$$

Knowing that the oxygen evolution reaction (OER) is an important half-reaction of the water-splitting reaction [8]. Wang et al. studied the Facile synthesis of Fe/

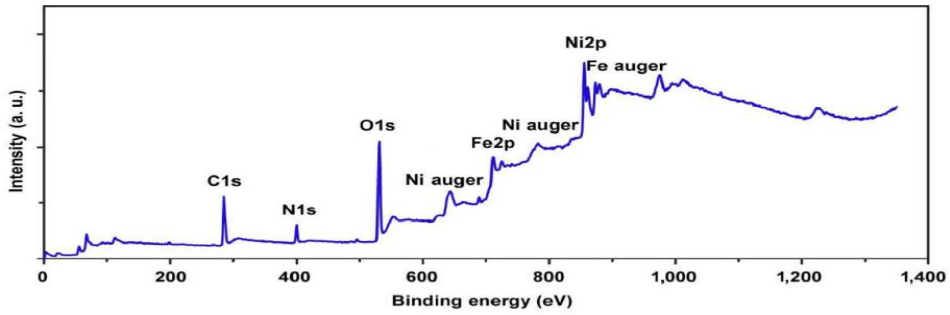

Figure 2: XPS survey spectrum of the Fe-Ni-Ox-NPs. Adapted from Nano Reseacrh. DOI: 10.1007/s12274-015-0881-0

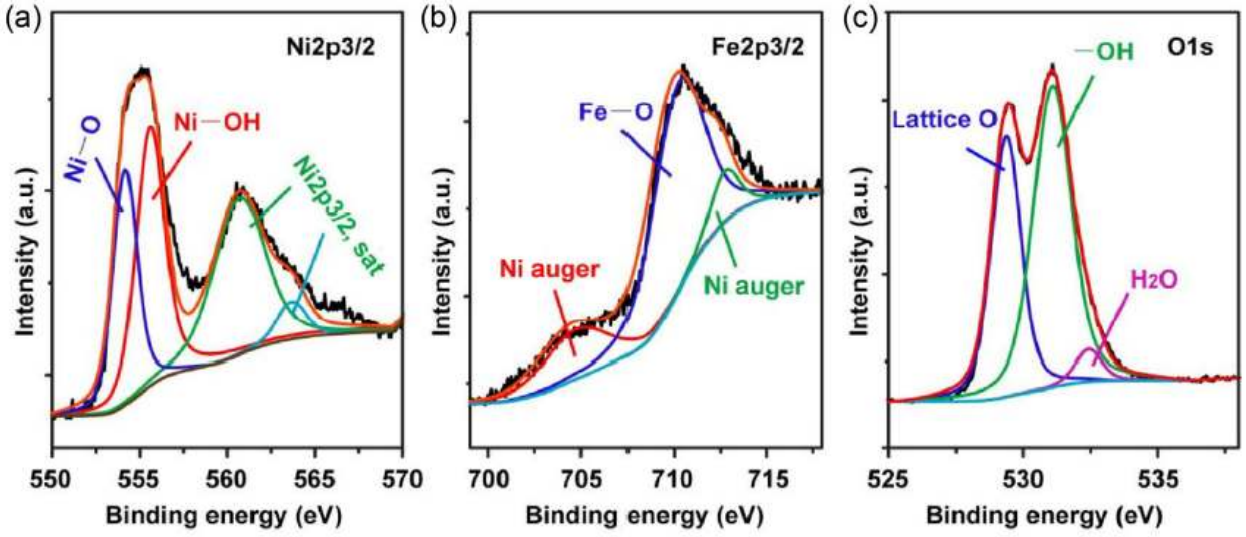

Figure 3: XPS spectra of (a) Ni2p3/2, (b) Fe2p3/2, and (c) O1s of Fe-Ni-Ox NPs. Adapted from Nano Research. DOI: 10.1007/s12274-015-0881-0

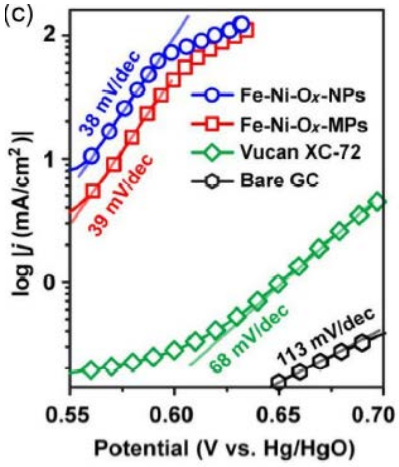

Figure 4: Tafel plots of Fe-Ni-Ox NPs (blue), Fe-Ni-Ox MPs (red), Vulcan® XC-72 carbon (green), and a bare glassy carbon electrode substrate (black) in 1 M KOH at a scanning rate of 10 mV/s. Adapted from Nano Research. DOI: 10.1007/s12274-015-0881-0

Ni bimetallic oxide solid-solution nanoparticles with superior electrocatalytic activity for the oxygen evolution reaction [9]. Modifying the aerosol spray-assisted approach produced amorphous Fe-Ni-Ox solid-solution nanoparticles (Fe-Ni-Ox-NPs), approximately, 20 nm in size by choosing iron/nickel acetylacetonates as raw materials instead of inorganic salts. The surface chemical environment analysis of the Fe-Ni-Ox NPs analysis was carried out using XPS as shown in Fig 2 and Fig 3 [10]. The fitted Ni2p3/2 spectra (Fig. 3(a)), shows that the surface Ni consisted of Ni–O and Ni–OH bonds indicating that the surface was adsorbed by hydroxyl. As for surface Fe (Fig. 3(b)), the Fe–O bond is dominant. Consistent with the chemical state of the surface metals, the surface O atoms comprised three types of oxygen: lattice O, –OH, and H_2O, with corresponding proportions of 38.6%, 57.3%, and 4.1%, respectively, as shown in Fig. 3. Kim et al. showed that there was a negative correlation between the relative

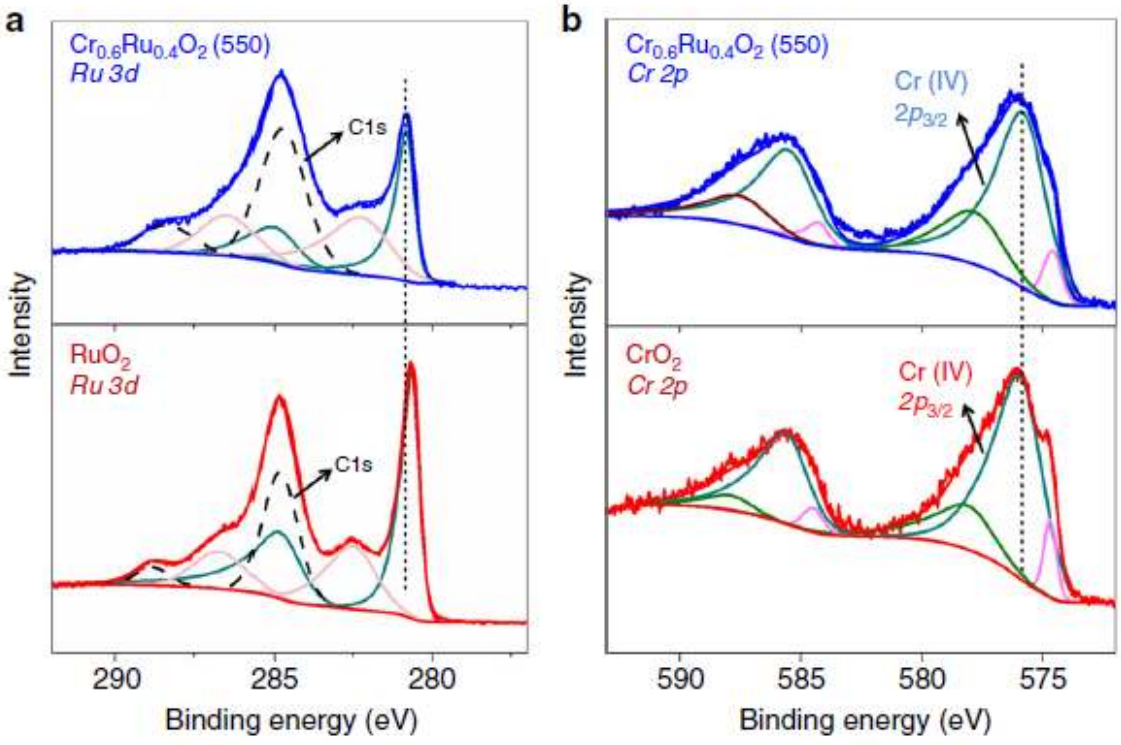

Figure 5: XPS of $Cr_{0.6}Ru_{0.4}O_2$ (550) for Ru 3d and Cr 2p. a XPS of $Cr_{0.6}Ru_{0.4}O_2$ (550) and RuO_2 for Ru 3d regions. b XPS of $Cr_{0.6}Ru_{0.4}O_2$ (550) and CrO_2 for Cr 2p regions. The blue and red smooth lines are fitting results of the sum of individual components. For Ru 3d, color codes are used to distinguish the different spin-orbit components, dark cyan for primary Ru $3d_{3/2}$ and $3d_{5/2}$ spin states, and light magenta for satellite Ru $3d_{3/2}$ and $3d_{5/2}$ spin states. Adapted from Nature Communications. DOI: 10.1038/s41467-018-08144-3.

concentrations of hydroxyl surface groups to the lattice oxygen and the Tafel slope of OER, and that approximately 70% –OH possession would decrease the Tafel slope to as low as 34 mV/dec [11]. Therefore, the lower –OH content is beneficial for obtaining a low Tafel slope for OER, which is in good agreement with the corresponding Tafel slope of 38 mV/dec in the subsequent electrochemical study. Furthermore, as shown in Fig. 4, the Tafel slopes (based on the Tafel equation: $\eta = a + b \log j$, where η represents the overpotential while a and b are constants) [12] for the Fe-Ni-Ox NPs (blue) and Fe-Ni-Ox MPs (red) are as low as 38 and 39 mV/dec, respectively, which are consistent with previous reports [13]. The low Tafel slopes indicate the low activation energy for electrochemical OER. In addition, the Tafel slopes of Vulcan® XC-72 carbon (green) black and the bare GC (black) electrode are as high as 68 and 113 mV/dec, respectively.

The work carried out by Lin et al. on Chromium-ruthenium oxide solid solution electrocatalyst for highly efficient oxygen evolution reaction in acidic media was discussed earlier [14]. Fig 5a demonstrates X-ray photoelectron spectroscopy (XPS) to access the surface chemical state of $Cr_{0.6}Ru_{0.4}O_2$ (550). It confirms that there are two sets of doublet peaks for Ru 3d in the region between 280 and 290 eV, corresponding to the doublet peaks for Ru (IV) $3d_{5/2}$, $3d_{3/2}$ and their satellite peaks [15]. The primary Ru $3d_{5/2}$ and $3d_{3/2}$ peaks of RuO_2 centered at 280.6 and 284.8 eV, respectively, are consistent with literatures [16]. A shift to higher binding energy can be clearly observed on $Cr_{0.6}Ru_{0.4}O_2$ (550) compared to RuO_2, suggesting a lower electron density at the Ru sites. This can be attributed to the electron withdrawing effect of Cr (IV) in the lattice. Note that the observed C1s peaks result from the carbon adhesive tape used in XPS measurement and environmental corrosion carbon. For Cr 2p, three sets of doublet peaks can be observed on $Cr_{0.6}Ru_{0.4}O_2$ (550) and CrO_2 in the region between 570 and 595 eV (Fig. 5b). The primary peaks at ~576.0 eV correspond to Cr (IV) $2p_{3/2}$ [17]. For Cr (IV) $2p_{3/2}$ of $Cr_{0.6}Ru_{0.4}O_2$ (550), a shift to lower binding energy is observed compared to CrO_2 implying a higher electron density at Cr sites, which confirms the withdrawing effect of Cr (IV) in $Cr_{0.6}Ru_{0.4}O_2$ (550). For the other two peaks in the Cr $2p_{3/2}$ region, the smaller ones at ~575.0 eV can be assigned to Cr (III) $2p_{3/2}$, which implies the appearance of a small amount of Cr (III) sites on the outer surface of $Cr_{0.6}Ru_{0.4}O_2$ (550) and CrO_2 crystals [17], and the

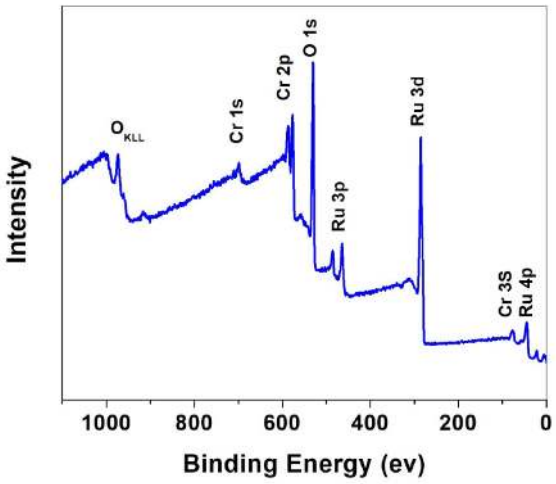

Figure 6: XPS wide-scan spectra of $Cr_{0.6}Ru_{0.4}O_2$(550). Adapted from Nature Communications. DOI: 10.1038/s41467-018-08144-3

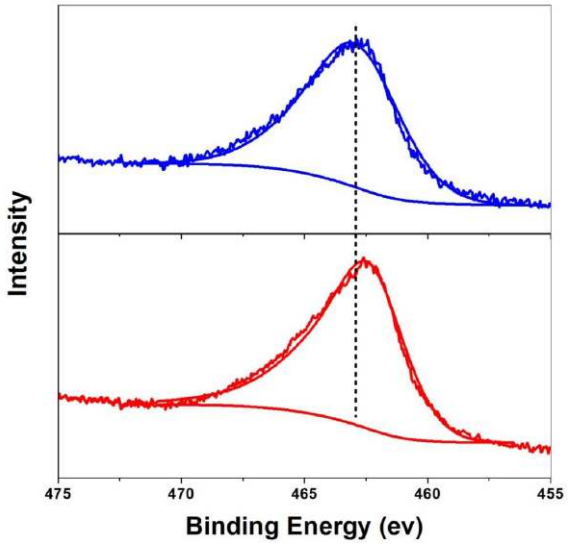

Figure 7: XPS spectra of $Cr_{0.6}Ru_{0.4}O_2$(550) (top) and RuO_2 (bottom) for Ru 3p. Adapted from Nature Communications. DOI: 10.1038/s41467-018-08144-3.

larger ones at ~577.9 eV can be assigned to CrO_2H, which likely resulted from the reaction between Cr (IV) and the proton from environment [18]. Additional XPS spectra for wide scan and Ru 3p regions are shown in figures 6 and 7.

3 Hydrogen Evolution Reaction

The hydrogen evolution reaction (HER, $2H^+ + 2e^- \rightarrow H_2$) is the cathodic reaction in electrochemical water splitting [19]. It is a classic example of a two-electron transfer reaction with one catalytic intermediate, and offers the potential to produce H_2, a critical chemical reagent and fuel. Achieving high energetic efficiency for water splitting requires the use of a catalyst to minimize the overpotential required to drive the HER. Platinum is the best known catalyst for HER and requires very small overpotentials even at high reaction rates in acidic solutions. However, the scarcity and high cost of Pt limits its widespread technological use. Advancement in research has shown the development of several earth-abundant HER catalysts, including sulfide- and phosphide- based materials with activities approaching that observed for platinum. The mechanism of HER is found in equation (10 – 12). Further research works have reported the use of solid solution as catalyst support or material for the synthesis of an electrocatalyst for efficient hydrogen evolution reaction.

$$H^+_{(aq)} + e^-_{(M)} \rightarrow H_{ads} \quad (10)$$

$$H^+_{(aq)} + H_{ads} + e^-_{(M)} \rightarrow H_{(g)} \quad (11)$$

$$H^+_{ads} + H_{ads} \rightarrow H_{2(g)} \quad (12)$$

Wang, Lu, et al. worked on $Mo_xW_{1-x}S_2$ solid solutions as 3D electrodes for hydrogen evolution reaction by investigating the electrocatalytic performance of $Mo_xW_{1-x}S_2$ ($0 \le x \le 1$) systems grown from 3D, free standing, interconnected glassy carbon foam to form a platform with different ratios of Mo and W in the $Mo_xW_{1-x}S_2$ solid solution [20]. In their work, they studied the morphology, elemental composition, bonding information, and electrocatalytic properties toward HER of 3D mixed MoS_2 and WS_2 samples. The composition and bonding information was obtained from XPS via wide scan and high-resolution spectroscopy for Mo3d and W4f. The wide scans for all samples are shown in Figure 8 and indicate that the substrate 3D carbon foam contains C and O and that no Mo and W are involved. XPS analysis demonstrates that, with an increasing amount of W precursor. there is a larger amount of W in the $Mo_xW_{1-x}S_2$ alloy. In addition, the detailed bonding information was studied by high-resolution XPS for Mo3d and W4f in Figure 7. For high resolution Mo3d spectra, the peaks at 229.3 and 232.4 eV indicate $Mo^{4+}\ 3d_{5/2}$ and $Mo^{4+}\ 3d_{3/2}$, respectively; and the peaks at 233.1 and 236.1 eV are caused by $Mo^{6+}\ 3d_{5/2}$ and $Mo^{6+}\ 3d_{3/2}$, respectively [21]. For the W4f spectra, the peaks shown at 33 and 35.1 eV indicate $W^{4+}\ 4f_{7/2}$ and $W^{4+}\ 4f_{5/2}$, respectively, and the peaks around 36.2 and 38.4 eV indicate $W^{6+}\ 4f_{7/2}$ and $W^{6+}\ 4f_{5/2}$, respectively [22]. The amount of Mo^{4+} and Mo^{6+} in the samples containing MoS_2 and the amount of W^{4+} and W^{6+} in the samples containing WS_2 are summarized in Table 1. There is a broadly increasing trend in the amount of W^{6+} along with the increasing ratio of WS_2 content. LSV

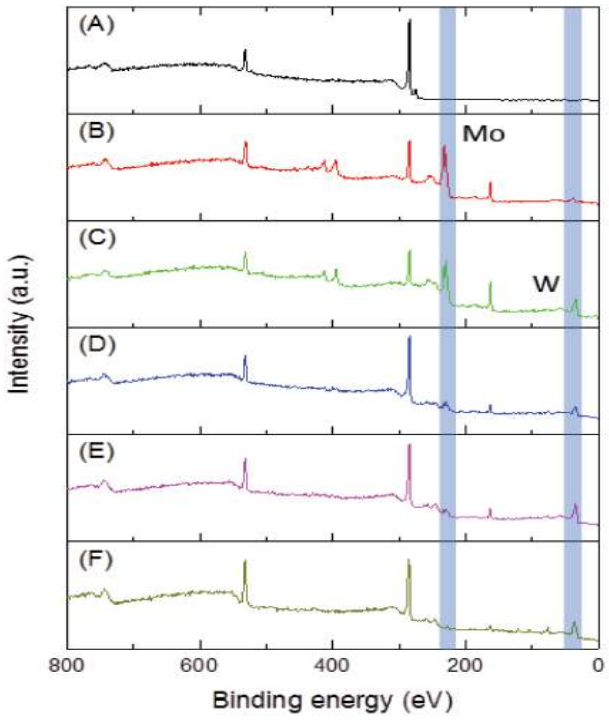

Figure 8: Wide scan XPS for A) carbon foam, B) pure MoS 2 -coated carbon foam, C) Mo $_{0.51}$W$_{0.49}$S$_2$ coated carbon foam, D) Mo $_{0.21}$ W $_{0.79}$ S $_2$ - coated carbon foam, E) Mo 0.14 W 0.86 S 2 -coated carbon foam, and F) pure WS 2 -coated carbon foam. Adapted from Advanced Materials Interfaces. DOI: 10.1002/admi.201500041

shows the electrocatalytic properties toward HER of 3D electrodes coated with Mo $_x$W$_{1-x}$S$_2$ alloy materials (fig 10). It shows a monotonic decrease of overpotential with an increasing amount of W (decreasing x) in the Mo x W$_{1-x}$ S$_2$ alloy.

Yang, Yufang, et al. synthesized and characterized a Ni-Co electrocatalyst for the hydrogen evolution reaction in acidic media [23]. This was done through electrodeposition of Ni-Co onto titanium substrates as a non-noble metal electrocatalyst. The Ni-Co showed higher catalytic properties and better stability. Ye, Ruquan, et al. in their work, studied High-Performance Hydrogen Evolution from a MoS$_{2(1-x)}$ P$_x$ Solid Solution [24]. They reported a one-step approach to improve the HER activity of MoS$_2$ and MoP via formation of a MoS$_{2(1-x)}$ P x (x = 0 to 1) solid solution, and demonstrated a simple method to improve the HER activity of transition metal semiconductors via the formation of a solid solution. Their work revealed that the HER activity of the solid solution can be further improved by increasing the surface area through employing MoS$_2$ nanoparticles as precursor or adding carbon black as a substrate. This suggests that there is still room for additional enhancement of the solid solution such as manipulating smaller sizes of MoS$_2$ precursor and using a high-surface-area heteroatom-alloyed carbon support [25]. Figure 11 d–f shows the chemical constituents of MoS $_{2(1-x)}$ P$_x$ which were further

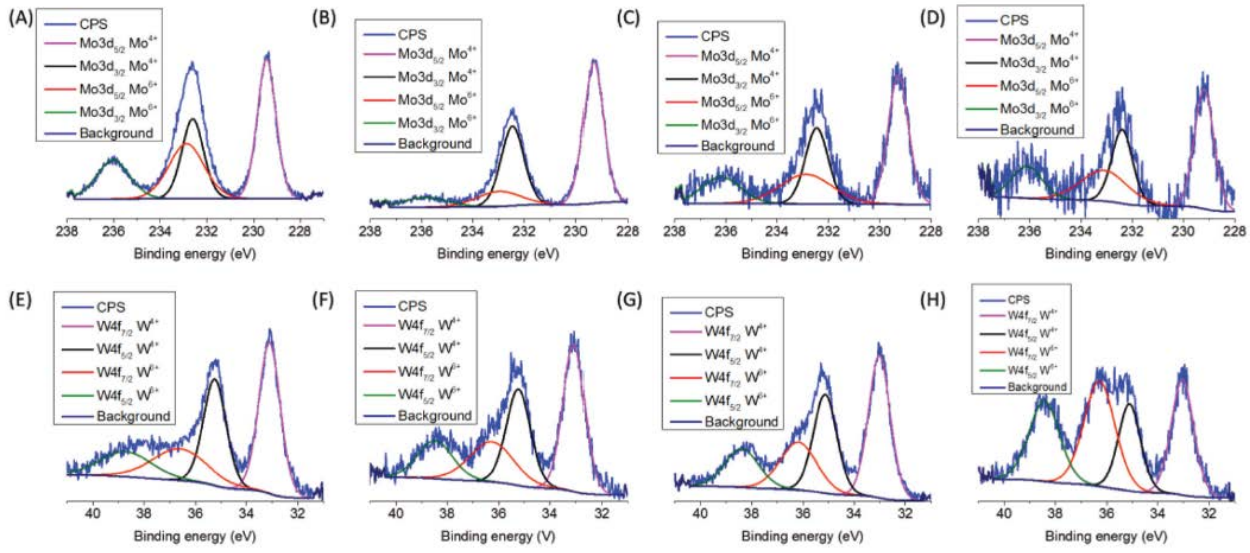

Figure 9: High-resolution XPS for Mo3d (higher row) and W4f (lower row) for A) pure MoS$_2$-coated carbon foam, B,E) Mo$_{0.51}$W $_{0.49}$ S$_2$ -coated carbon foam, C,F) Mo $_{0.21}$W $_{0.79}$ S$_2$ -coated carbon foam, D,G) Mo $_{0.14}$ W$_{0.86}$ S$_2$-coated carbon foam, and H) pure WS$_2$ -coated carbon foam. Adapted from Advanced Materials Interfaces. DOI: 10.1002/admi.201500041

Table 1: Bonding information for as-prepared 3D TMDs. Adapted from Advanced Materials Interfaces. DOI: 10.1002/admi.201500041

Bonding Information	MoS_2 [%]	$Mo_{0.51}W_{0.49}S_2$ [%]	$Mo_{0.21}W_{0.79}S_2$ [%]	$Mo_{0.14}W_{0.86}S_2$ [%]	WS_2 [%]
Mo^{4+}	57.3	80.4	62.6	61.5	0
Mo^{6+}	42.7	19.6	37.4	38.5	0
W^{4+}	0	65.1	63.7	64	44
W^{6+}	0	34.9	36.3	36	56

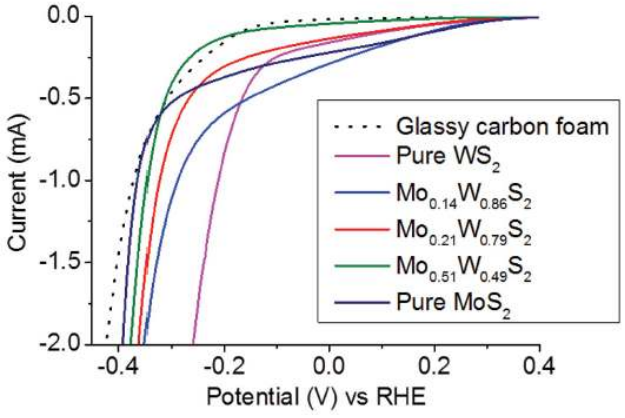

Figure 10: LSV of glassy carbon foam and prepared pure MoS 2 , Mo 0.51 W 0.49 S 2 , Mo 0.21 W 0.79 S 2 , Mo 0.14 W 0.86 S 2, and pure WS 2 coated carbon foam in 0.5 M H 2 SO 4 at a scan rate of 2 mV s –1. Adapted from Advanced Materials Interfaces. DOI: 10.1002/admi.201500041

investigated by X-ray photoelectron spectroscopy (XPS) and X-ray diffraction (XRD).

4 Oxygen reduction reaction

In the mechanism of the oxygen reduction reaction, it is important to note that ORR in aqueous solutions occurs mainly by two pathways (equation 13-18): the direct four-electron transfer pathway from O_2 to H_2O, and the two-electron transfer pathway from O_2 to hydrogen peroxide (H_2O_2) [26]. In nonaqueous aprotic solvents and/or in alkaline solutions, the one-electron transfer pathway from O_2 to superoxide (O^{2-}) could also occur. ORR kinetics is, normally, very slow. In order to speed up the ORR kinetics to reach a practical usable level in a fuel cell, a cathode ORR catalyst is needed. Platinum based materials are the remarkable, practical catalysts. However, the high cost of platinum has hindered the commercialization and widespread application of ORR technologies. Ongoing, thorough research to replace platinum based materials with earthly abundant materials such as transition metal macrocyclic compounds, transition metal chalcogenides, and transition metal carbides progress has been made. Further research has also shown that solid solutions, when used as catalyst support or material for synthesizing electrocatalyst, result in an efficient oxygen reduction reaction. Yige Zhao and his team studied Pt–Co secondary solid solution nanocrystals supported on carbon as next-generation catalysts for the oxygen reduction reaction [27]. They reported a novel sort of secondary solid solution nanocrystals via heat treatment of their primary solid solution supported on carbon black and fabricated Pt–Co secondary, solid solution nanocrystals with long-range ordered intermetallic $CoPt_3$ as the solvent and Co as the solute. Their activities with the oxygen reduction reaction reveals a volcano-type dependence on Co solid solubility, and the best Co-10% secondary solid solution catalyst displays a remarkable increase in ORR activity compared to commercial Pt/C (E-TEK). X-ray photoelectron spectroscopy (XPS) experiments were conducted on secondary solid solution (Co-10%), intermetallic $CoPt_3$ and commercial Pt/C, respectively. Considering that the Co 2p peaks are very weak owing to the very low Co solubility in the $CoPt_3$ compound (Fig. 1) and that the active sites for the Pt–Co secondary solid solution alloys are Pt atoms rather than Co atoms, the influence of the electronic structure will be explained by the analysis of Pt 4f peaks. Shi, Meiqin, et al carried out an experiment on Enhanced Electrocatalytic Oxygen Reduction on NiWO*x* Solid Solution with Induced Oxygen Defects [28]. They developed an efficient strategy for the synthesis of the solid solution NiWOx system by using $W_{18}O_{49}$ as precursors. The electrochemical studies revealed that, compared to the Pt/$W_{18}O_{49}$ and commercial 20 wt% Pt/C, the obtained Pt/NiWOx exhibited not only enhanced ORR electrocatalytic activity but also superior stability in alkaline media which renders them a class of high performance catalyst for ORR. They stated that the influence of Ni induced defects on the electronic structure of surface/near-surface of NiWOx solid solution was examined by X-ray photoelectron spectroscopy (XPS). The full-range XPS spectrum of NiWOx solid solution show the elements W, Ni, O and also some carbon due to surface

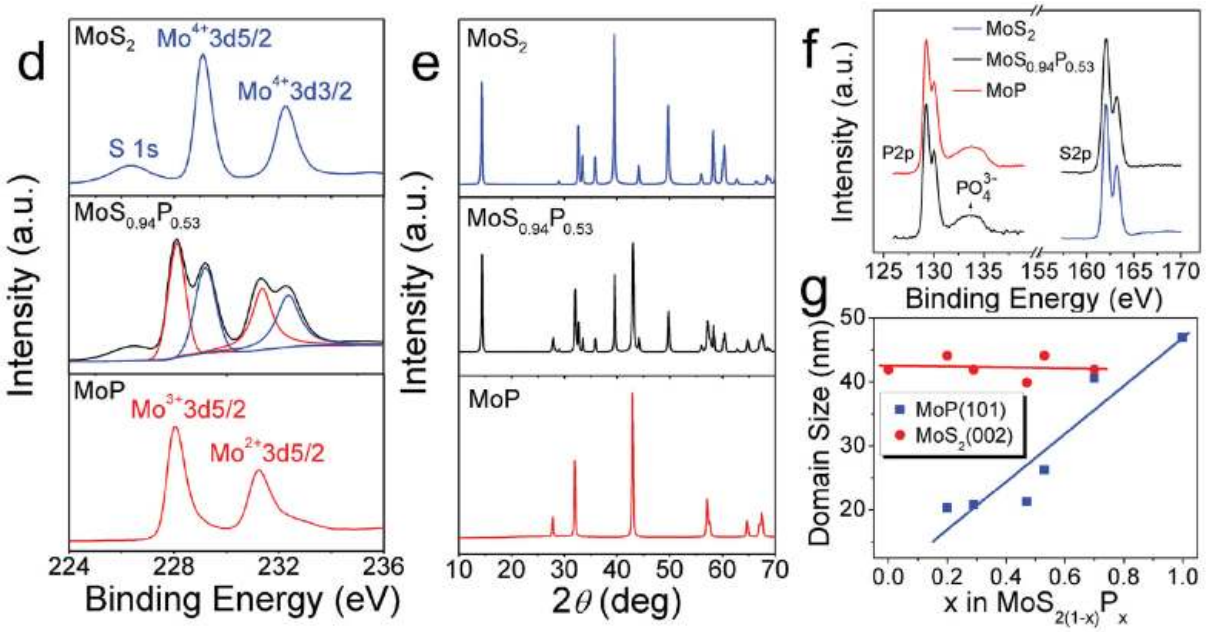

Figure 11: Structure characterization of $MoS_{2(1-x)}P_x$. SEM images of a) MoS_2, b) $MoS_{0.94}P_{0.53}$, and c) MoP. The scale bars are 10 μm. d) High resolution XPS spectra of Mo3d. e) XRD spectra of MoS_2, $MoS_{0.94}P_{0.53}$, and MoP. f) High resolution XPS P2p and S2p spectra of MoS_2 (blue line), $MoS_{0.94}P_{0.53}$ (black line), and MoP (red line). g) Domain sizes of MoS_2 (002) plane and MoP (101) plane in $MoS_{2(1-x)}P_x$. Adapted from Advanced Materials. DOI: 10.1002/adma.201504866

contamination (Fig 14). More detailed information on the chemical state of these elements can be obtained from the high-resolution XPS spectra of W 4f and Ni 2p, as shown in Figure 15b and c. Figure 15d shows the measured Raman scattering spectra of pristine $W_{18}O_{49}$ and NiWOx solid solution samples. For the W 4f (fig 15b), the core-level spectrum can be deconvoluted into three doublets which are associated with different oxidation states of surface W atoms. Also, the XPS Ni 2p3/2 spectrum was analyzed as three components at 855.7 eV, 856.5 eV and 857.9 eV, corresponding to NiO, $Ni(OH)_2$ and NiOOH, respectively, with both W 4f and Ni2p3 having fitted results marked in red lines.

4.1 Thermodynamics and Kinetics of Oxygen Reduction Reaction

General Principles. The standard reduction potential of O_2 to OH^-, $E_{O2/OH^-}{}^0$, is 0.401 V versus Standard Hydrogen Electrode (SHE) for the direct four-electron pathway [29]:

$$O_2 + H_2O + 4e^- \rightleftharpoons 4OH^- ; E^0 = 0.401V \text{ vs SHE} \quad (13)$$

In an alternative two-electron pathway, O_2 is reduced to peroxide ion

$$O_2 + H_2O + 2e^- \rightleftharpoons OH_2^- + OH^- ; E^0 = -0.076V \text{ vs SHE} \quad (14)$$

followed by either further reduction

$$HO^{2-} + H_2O + 2e^- \rightleftharpoons 3OH_2^- ; E^0 = 0.878V \text{ vs SHE} \quad (15a)$$

or disproportionation

$$2HO^- \rightleftharpoons 2OH^- + O_2 \quad (15b)$$

In acidic solutions, the four-electron (Reaction 16) and two electron (Reactions 17, 18a, and 18b) pathways are

$$O_2 + 4H^+ + 4e^- \rightleftharpoons 2H_2O ; E^0 = 1.229V \text{ vs SHE} \quad (16)$$

$$O_2 + 2H^+ + 2e^- \rightleftharpoons 2H_2O_2 ; E^0 = 0.695V \text{ vs SHE} \quad (17)$$

$$H_2O_2 + 2H^+ + 2e^- \rightleftharpoons 2H_2O ; 1.776V \text{ vs SHE} \quad (18a)$$

$$2H_2O_2 \rightleftharpoons 2H_2O + O_2 \quad (18b)$$

He, Guanjie, et al. intensively worked on solid solution nitride/carbon nanotube hybrids to enhance electrocatalysis of oxygen in zinc-air batteries [30] and synthesizing and designing Ni/Co nitrides ($Ni_xCo_{3-x}N$) solid-solutions decorated on nitrogen doped carbon nanotubes (NCNT) as highly stable bi-functional ORR and OER electrocatalysts for Zn-air batteries. The as-synthesized,

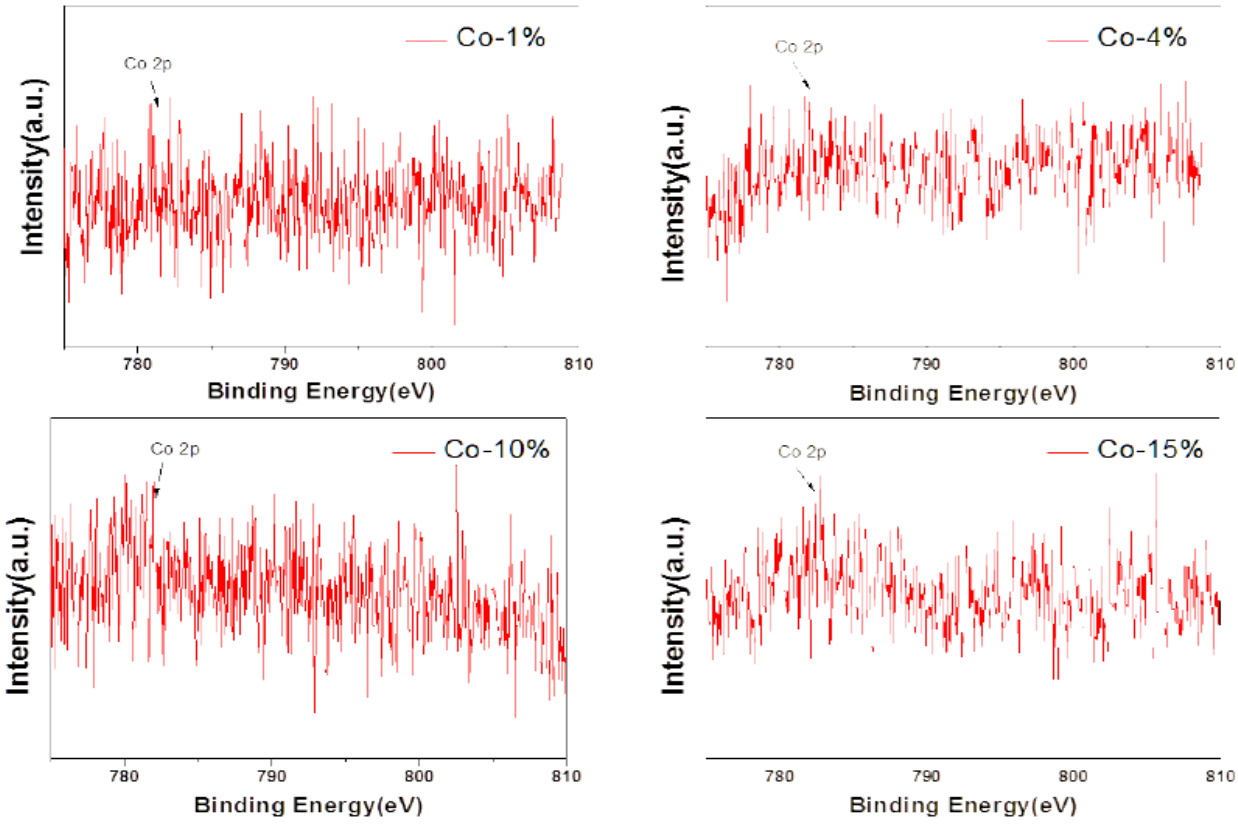

Figure 12: High resolution XPS spectra showing Co 2p peaks. Adapted from the Royal Society of Chemistry, Journal of Materials Chemistry. DOI: 10.1039/C5TA05888K

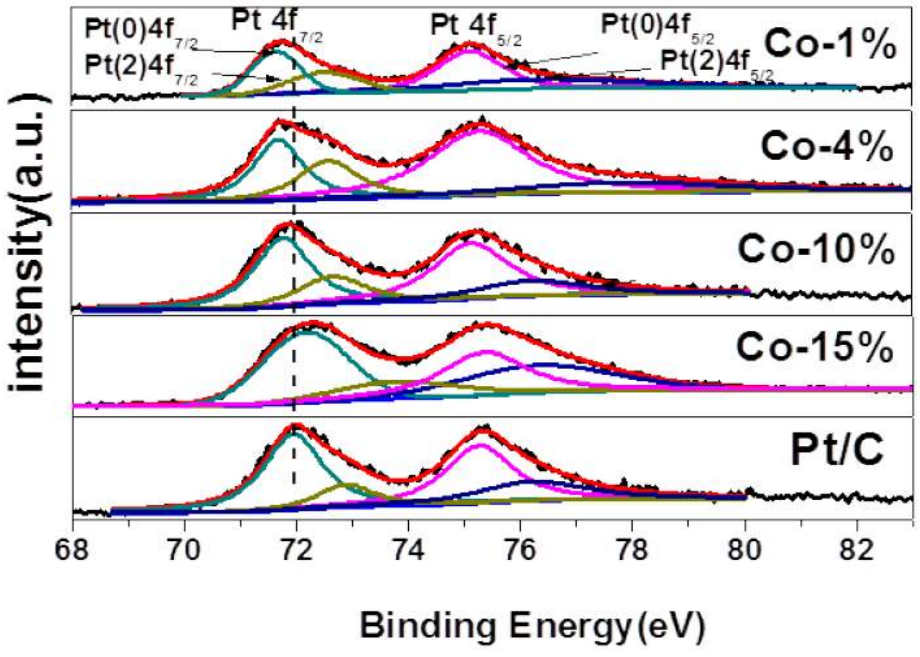

Figure 13: High resolution XPS spectra showing Pt 4f peaks of all the secondary solid solution catalysts. Adapted from the Royal Society of Chemistry, Journal of Materials Chemistry. DOI: 10.1039/C5TA05888K

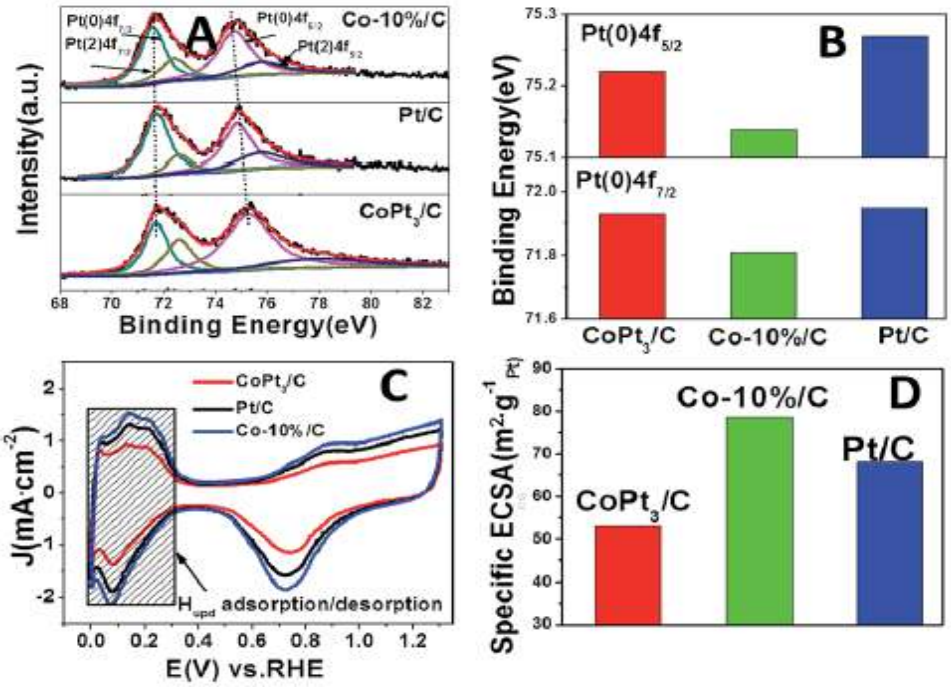

Figure 14: High resolution XPS spectra showing Pt 4f peaks; (B) the fitted Pt(0) 4f5/2 and Pt(0) 4f7/2 core-level binding energies; (C) CV curves; (D) the calculated specific ECSA using the data of (C). Adapted from the Royal Society of Chemistry, Journal of Materials Chemistry. DOI: 10.1039/C5TA05888K

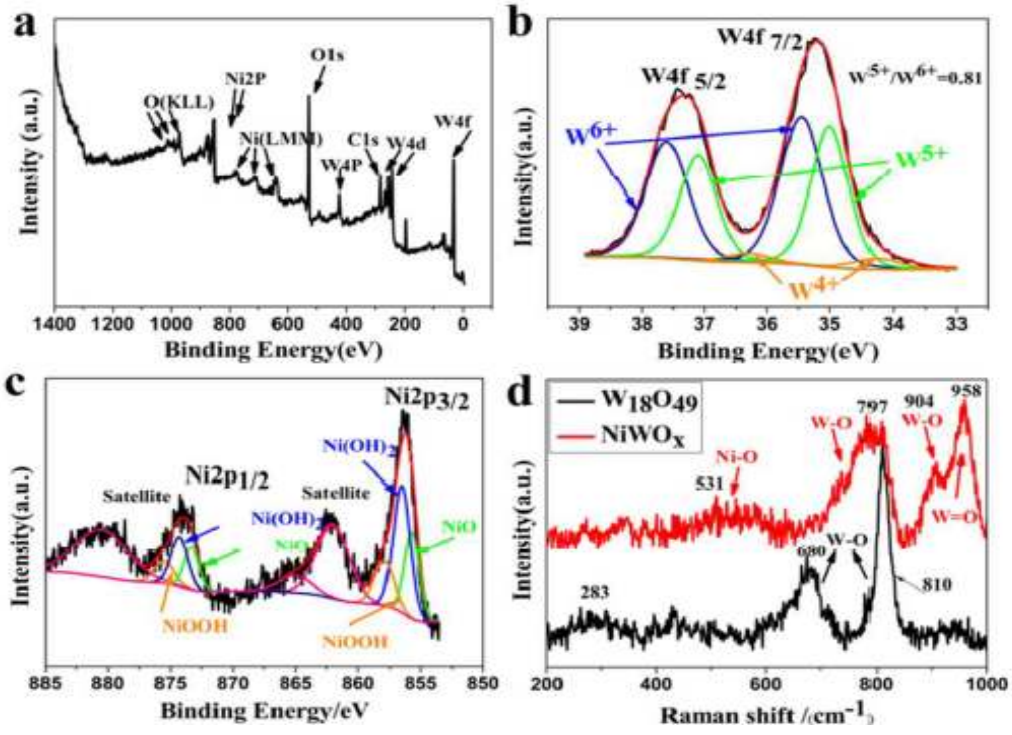

Figure 15: XPS spectra of the as-prepared NiWOx solid solution electrocatalyst for ORR a) Full spectra b) W 4f and c) Ni 2p d) the Raman scattering spectra of pristine $W_{18}O_{49}$ and NiWOx. Adapted from the American Chemical Society, applied Materials and Interfaces. DOI: 10.1021/acsami.7b1089

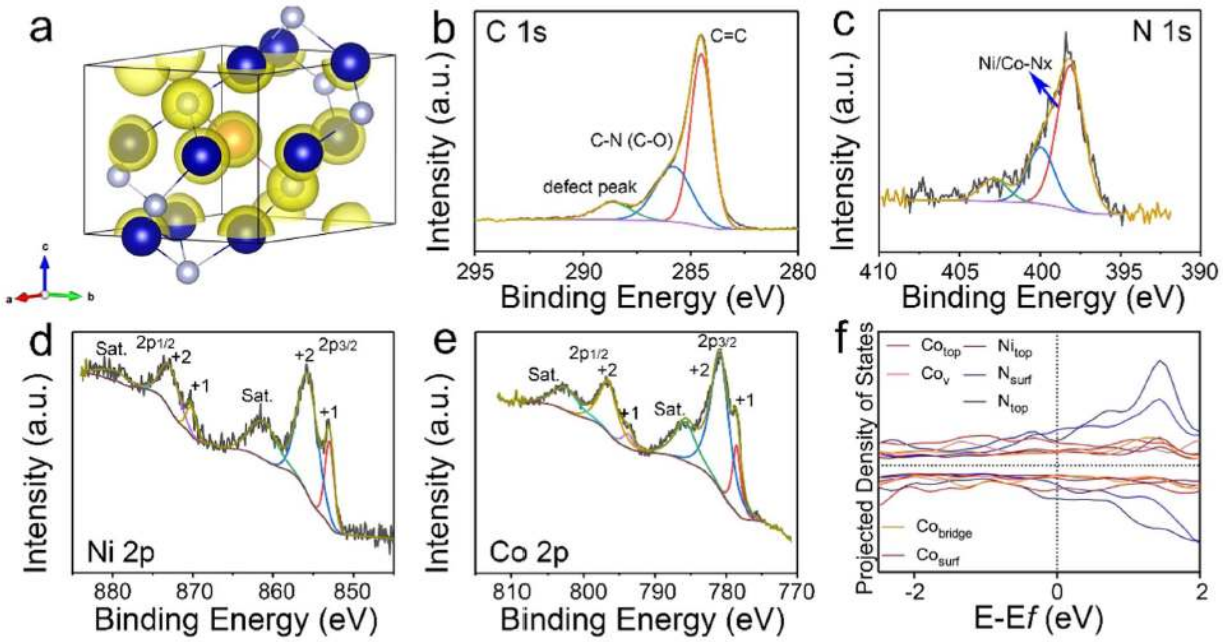

Figure 16: (a) The charge distribution of the Fermi level of $Ni_{0.5}Co_{2.5}N$. The isosurface is set to $0.2e/r0^3$, where r0 is the Bohr radii. The salmon, blue and grey balls represent Ni, Co, and N atoms, respectively; XPS spectrum for SS/NCNT sample of (b) C 1s; (c) N 1 s; (d) Ni 2p and (e) Co 2p, respectively. (f) The projected density of states of the surface atoms of $Ni_{0.5}Co_{2.5}N$ (111) surface. Adapted from Elsevier, Energy Storage Materials. DOI: 10.1016/j.ensm.2018.08.020

catalysts demonstrated superior catalytic properties to commercial noble-metal based counterparts, i.e. platinum, on a carbon support for ORR and iridium oxide for OERand much enhanced stability. The charge distribution of $Ni_{0.5}Co_{2.5}$ at Femi level displayed the behavior of the metallic bonding (fig 16a). Also, Fig 16b-f gives the experimental confirmation of the chemical compositions and valence states of SS/NCNT using X-ray photoelectron spectroscopy (XPS). As illustrated in Fig. 5b, the C 1 s peak shows carbon-nitrogen (and oxygen) bonds at ~285.6 eV, indicating successful nitrogen doping of defect-rich carbon nanotubes [31]. It is widely known that nitrogen-doped carbon materials can be beneficial for oxygen electrocatalysis [32]. In addition, the N 1 s region (Fig. 16c) shows peaks at 400 and 402.9 eV that correspond to absorbed N_2, interstitial nitrogen dopants and oxidized surface nitrogen, respectively, on NCNT [33,34]. The strong peak at ~398.1 eV corresponds to the metallic Ni/Co and nitrogen bonds [35]. The Ni 2p region (Fig. 16d) shows a multiplet split Ni 2p3/2 peak (centered at ~873.4 and ~870.3 eV), a multiplet split Ni 2p1/2 peak (~855.6 and ~852.5 eV) and a pair of satellite peaks (ΔNi=17.8 eV), which correlates to the mixed valence states of +2 and +1 Ni at the material surface. Fig. 16e demonstrates the Co 2p region. Similar to Ni 2p region, the Co 2p peaks also contains spin-orbit doublets (ΔCo=15.0 eV). The doublets consist of two pairs of peaks and one pair of satellite peaks in lower (Co 2p3/2) and higher (Co 2p1/2) energy bands centered at 803.0 and 785.9 eV, respectively, suggesting the same varied valence states as Ni. The atomic ratio of metal to nitrogen on the material surface, as measured by XPS, was 2.6: 1. This was substantially lower than the metal to oxygen ratio (~11: 1), suggesting negligible oxidation of the metal nitride surface under ambient conditions.

5 Overall water splitting (HER+OER)

Photocatalytic water splitting over semiconductors without the use of any electron sacrificial agents is important to the conversion of solar energy into chemical energy [36]. Ye, Hui-Fang, et al. extensively studied P-doped $Zn_xCd_{1-x}S$ solid solutions as photocatalysts for hydrogen evolution from water splitting coupled with photocatalytic oxidation of 5-hydroxymethylfurfural [37]. They reported a remarkable photocatalytic hydrogen production from pure water without the assistance of electron sacrificial agents by using P-doped Zn_xCd_{1-xS} with rich S vacancies ($Zn_xCd_{1-x}S$-P) as the photocatalyst. Weiren et al. developed a new type of 3D metal-vacancy solid-solution NiAlP nanowall arrays synthesized by a combination of selective alkali-etching and phosphorization strategies as a highly-active and earth-abundant, all-pH, bifunctional electrocatalyst for efficient overall water splitting [38]. In the same vein, Bhadram et al. worked on $Zn_xMn_{1-x}O$ solid solutions in

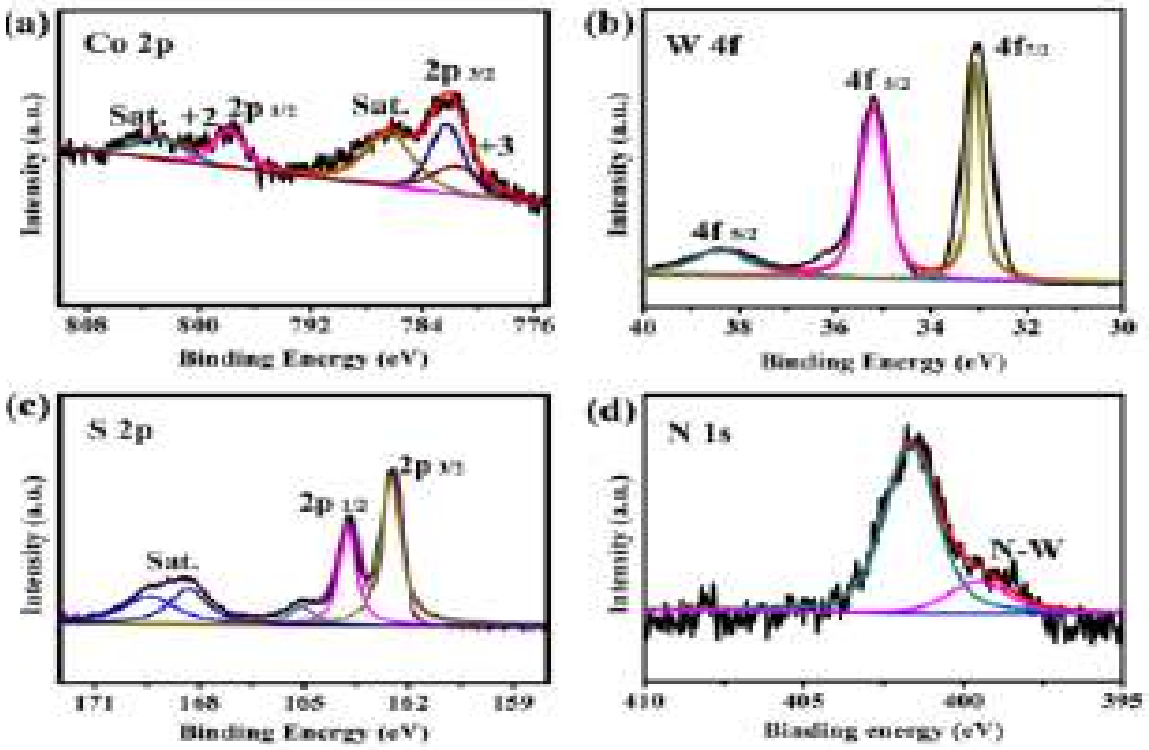

Figure 16: (a-d) The high-resolution XPS spectrum of Co 2p, W 4f, S 2p and N 1s of the N-$Co_xW_{1-x}S_2$ ultra-thin nanoflakes (Sat. means shake-up satellite.). Adapted from Journal of Physical Chemistry Chemical Physics, Royal Society of Chemistry. DOI: 10.1039/C7CP01684K

the Rocksalt Structure: Optical, Charge transport, and photoelectrochemical properties [39], which produced solid solutions of $Zn_xMn_{1-x}O$, with x = 0.5 and 0.3 in the metastable rocksalt phase using high-pressure and high-temperature (HPHT) techniques. Lardhi et al. investigated the properties of layered oxychalcogenides MCuOCh (M = trivalent Bi, Y, Sc or lanthanide ions; Ch = S, Se, Te) for water splitting [40]. In their investigation, they simulated the solid solutions $Bi1_xRE_xCuOS$ (RE = Y, La, Gd and Lu) from pure BiCuOS (Eg B 1.1 eV) to pure RECuOS compositions (Eg B 2.9 eV) by DFT calculations based on the HSE06 range-separated hybrid functional with the inclusion of spin–orbit coupling.

Wan and his colleagues prepared a facile method to develop a nitrogen anion-decorated cobalt tungsten disulfide solid solutions, retaining ultra-thin WS_2-like nanosheet structures (N–$CoxW_{1-}xS_2$) anchored on carbon nanofibers (CNFs) through a combination of electrospinning and post carbonization [41]. They reported that the as-prepared catalyst can be directly used as the binder-free electrode for the HER application [42]. Stating categorically that the composite catalyst displays a low overpotential of 93 mV to reach a current density of 10 mA/cm^2 and excellent long-term stability. The synergistic effect of the WS_2 nanosheets gives a secure framework for stabilizing the amorphous Co–S clusters; CNFs substrate and nitrogen anion-decoration greatly improves the inherent conductivity of the catalyst, resulting in a significantly promoted hydrogen evolution reaction activity and stable performance compared to pure Co_9S_8 nanoparticles or ultra-thin WS_2 nanosheets [43]. The N–$CoxW_{1-}xS_2$ electrode demonstrates excellent electrocatalytic performance with a current density of 10 mA cm^{-2} at a low overpotential of 93 mV and Tafel slope of 85 mV dec^{-1} as well as long-term stability in acid electrolyte [44].

The analysis of the composition and chemical states of N-$Co_xW_{1-x}S_2$ nanosheets and the obtained XPS spectra of Co 2p, W 4f, S 2p and N 1s are shown in Figure 16a. The Co 2p spectrum displays two doublets of Co^{3+} and Co^{2+}, and two satellites matching well with the reported values of Co 2p [45]. The W 4f spectrum displays two sharp peaks at 33.0 and 35.2 eV attributed to the 4f7/2 and 4f5/2 of orbitals W4+ (Figure 16b) [46]. Meanwhile, Figure 16c displays the double major peaks and one shake-up satellite peak appearing at 162.5, 163.7 and 168.5 eV, which are ascribed to the S 2p3/2 and S 2p1/2, respectively. Figure 16d shows

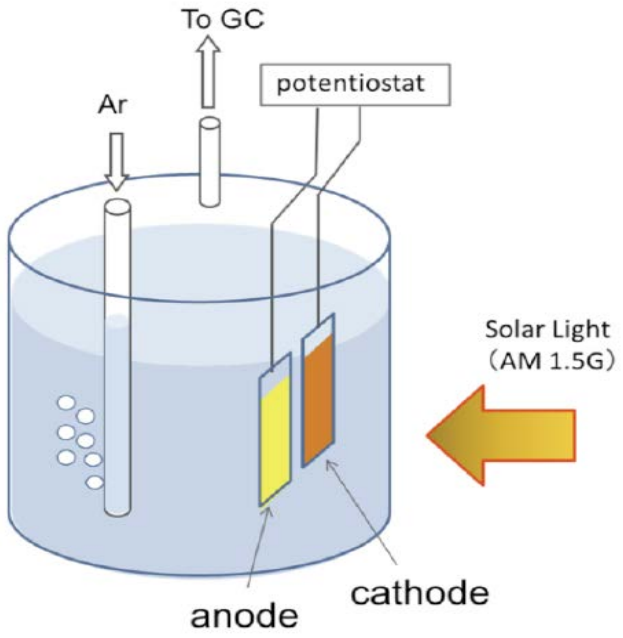

Figure 17: (a) Photoelectrochemical system equipped with on-line gas chromatography, two-electrode type. The photoanode and photocathode existed side by side in the same plane. (b) Photograph of Pt/TiO_2/CdS/CGIZS/Au photocathode (0.231 cm^2) and CoFeOx/$BiVO_4$/ITO photoanode (0.272 cm^2) used for overall water splitting. Adapted from Sustainable Energy and Fuels, Royal Society of Chemistry. DOI: 10.1039/x0xx00000x.

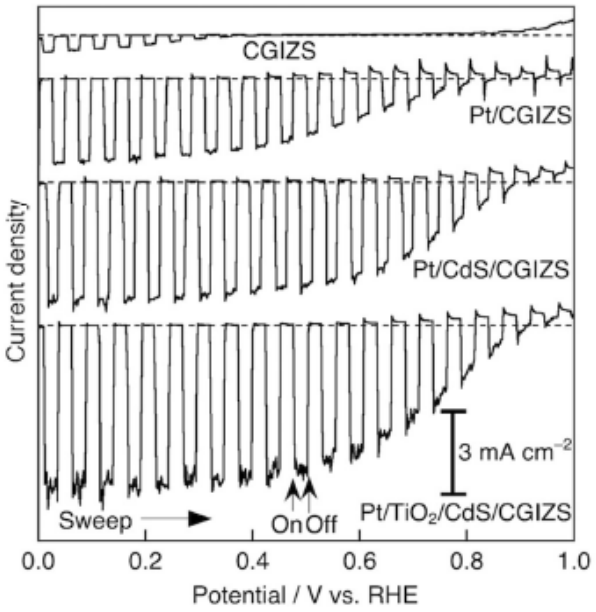

Figure 18: I-V curves of CGIZS photoelectrodes with various surface modifications under simulated sunlight. CGIZS represents $Cu_{0.8}Ga_{0.4}In_{0.4}Zn_{0.4}S_2$ (Ga 20-30% excess) prepared by a flux method using LiCl-KCl (3:2) mixture at 823 K for 15 h. Electrolyte, aqueous phosphate buffer solution (0.5 mol L^{-1} of Na_2SO_4 + 0.25 mol L^{-1} of NaH_2PO_4 + 0.25 mol L^{-1} of Na_2HPO_4) with pH 6.4; light source, solar simulator (AM 1.5G). Adapted from Sustainable Energy and Fuels, Royal Society of Chemistry. DOI: 10.1039/x0xx00000x

the N 1s spectrum with two peaks, where the N-W bond is distinctly detected at 398.1 eV demonstrating the presence of N in an obtained solid solution [47].

Hayashi et al. showed that $(CuGa_{1-y}In_y)_{1-x}Zn_{2x}S_2$ (CGIZS)-based photocathodes fabricated with a particle transfer method exhibited a photocurrent of 4.5 $mAcm^{-2}$ at 0.6 V vs. RHE along with a largely positive onset potential of 1.0 V vs. RHE under simulated sunlight (AM 1.5G) and the initial solar-to-hydrogen energy conversion efficiency of 1.1% was obtained with photoelectrochemical water splitting using a two-electrode cell composed of the CGIZS-based photocathode and a $BiVO_4$-based photoanode [48] (Fig. 17). Their work reported that $Cu_{0.8}Ga_{0.4}In_{0.4}Zn_{0.4}S2$ (x=0.2, y=0.5) photocatalyst powder was prepared successfully as a micrometer-sized single phase crystal by a flux method using LiCl-KCl molten salt (melting point: 625 K at the molar ratio 3:2). Figure 18 shows the I-V curves under chopped simulated sunlight (AM 1.5G) for $Cu_{0.8}Ga_{0.4}In_{0.4}Zn_{0.4}S_2$ (x=0.2, y=0.5 and Ga 30% excess)-based photoelectrodes with various surface modifications. The PEC water splitting was conducted using a two electrode system in a one-pot flask with no bias under irradiation of simulated sunlight (Fig. 17). The gas detection was carried out to confirm if the water splitting proceeds using the two-

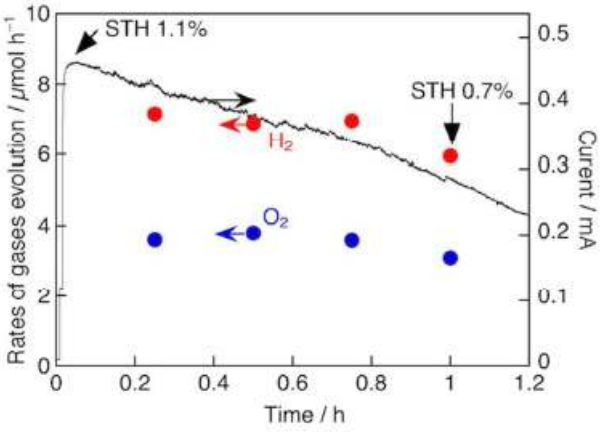

Figure 19: PEC water splitting by using the Pt/TiO_2/CdS/CGIZS photocathode (geometric area, 0.231 cm^2) and a CoFeOx/$BiVO_4$ photoanode (geometric area, 0.272 cm^2) under simulated sunlight irradiation. The CGIZS represents $Cu_{0.8}Ga_{0.4}In_{0.4}Zn_{0.4}S_2$ (Ga 20% excess) prepared by a flux method at 823 K for 15 h. Electrolyte, aqueous phosphate buffer solution (0.5 mol L^{-1} of Na_2SO_4 + 0.25 mol L^{-1} of NaH_2PO_4 + 0.25 mol L^{-1} of Na_2HPO_4) with pH7.0 adjusted by KOH; light source, solar simulator (AM 1.5G). Adapted from Sustainable Energy and Fuels, Royal Society of Chemistry. DOI: 10.1039/x0xx00000x

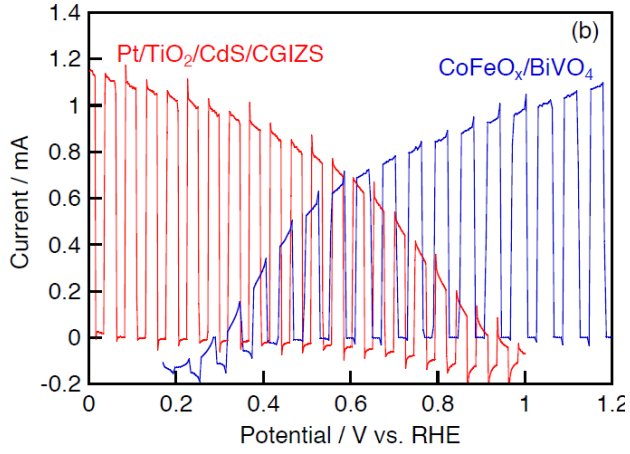

Figure 20: Current-potential curves of $Pt/TiO_2/CdS/CGIZS$ and $CoFeOx/BiVO_4$ photoelectrodes under simulated sunlight irradiation. In (b), the irradiated areas of $Pt/TiO_2/CdS/CGIZS$ and $CoFeOx/BiVO_4$ were considered to be 0.231 and 0.272 cm^2 . Electrolyte, aqueous phosphate buffer solution (0.5 mol L^{-1} of Na_2SO_4 + 0.25 mol L–1 of NaH_2PO_4 + 0.25 mol L^{-1} of Na_2HPO_4) with pH 7.0; light source, solar simulator (AM 1.5G). Adapted from Sustainable Energy and Fuels, Royal Society of Chemistry. DOI: 10.1039/x0xx00000x

electrode system, as shown in Figure 19. The observed photocurrent of 0.46 mA at the beginning stage, and the value was not very far from the expected photocurrent of 0.67 mA (Fig. 20). Table 2 shows the current densities and onset potentials estimated from J-V curves of various Pt/CdS/CGIZS/Au photoelectrodes under simulated sunlight. Also, Table S1 demonstrates current densities and onset potentials in J-V curves of various CGIZS photocathodes (Pt/CdS/CGIZS/Au) with excess elements under chopped simulated sunlight (AM 1.5G)

6 Electrocatalysis of Carbondioxide Reduction

Electrochemical reduction of CO_2 has a potential of becoming a major contributor to sustainable production of fuels and chemicals through the use of renewable CO_2 free energy sources. However, the development of an effective catalyst is vital, as there are currently no industrial scale operations that utilize this technology due to low energetic efficiency. Lardhi et al. worked on electrodeposited Cu-Sn alloy for electrochemical CO_2 reduction to $CO/HCOO^-$. The group successfully prepared Cu-Sn alloy electrodes by the simple electrodeposition method for the electrochemical reduction of CO_2 into CO and $HCOO^-$ [41]. They reported that the alloy electrode surfaces provided good selectivity and efficiency in electrochemical CO_2 conversion because they provided appropriate binding energies between the metal and the reactive species obtained through CO_2 reduction. Their work shows that the Cu-Sn alloy can control product selectivities of CO and $HCOO^-$ by altering the alloy composition. Fig. 21 shows the XPS analysis of the chemical bonding states of Cu 2p and Sn 3d in the alloys before and after CO_2 reduction. Fig 22 shows the Faradaic efficiency of CO_2 electroreduction products as a function of potential and Fig 23 shows the total current density for CO_2 electroreduction as a function of potential on Cu_{100}, $Cu_{87}Sn_{13}$, $Cu_{76}Sn_{24}$, $Cu_{55}Sn_{45}$, and $Sn_{100.}$ Electrodeposition conditions of various catalysts using AES measurements are shown in Table 3. The relative composition ratios on the surfaces of the prepared catalysts using AES measurements are shown in Table 4.

Chen et al. studied Au as a cocatalyst loaded on solid solution $Bi_{0.5}Y_{0.5}VO_4$ for enhancing photocatalytic CO_2 reduction activity [49]. Their work stated that Au as a cocatalyst was deposited on the surface of solid solution $Bi_{0.5}Y_{0.5}VO_4$ by a photo-deposition method for photocatalytic reduction of CO_2. The deposited gold particles on the surface of the $Bi_{0.5}Y_{0.5}VO_4$ enhanced the catalytic activity. Then, the as-synthesized samples were used as a photocatalyst for CO_2 conversion with H_2O as an electron donor. Fig. 24 shows an XPS image which confirms the surface element composition of as-prepared samples and valence state of the Au species. It can be seen in the XPS survey spectra (fig. 24a) that Bi, Y, V, O and Au binding energy peaks were detected. Fig. 24b also reveals that the binding energies of Au $4f_{7/2}$ and $4f_{5/2}$ were found to be 83.6 and 87.2 eV, respectively, corresponding to metallic Au (Au^0) [50]. Fig. 25a shows the rates of CO evolution on BYV with different Au loading contents along with irradiation time. From Fig. 25a, for bare BYV, the rate of CO evolution is about 0.07 $\mu mol.g^{-1}.h^{-1}$, suggesting that BYV has the ability to reduce CO_2 to CO because of the position of conduction band being higher than the reduction potential of CO evolution. The photocatalytic emission spectra of the samples were measured in order to uncover the influence of Au cocatalyst on the charge separation, as shown in Fig. 25b. The spectra indicate that the Au loaded BYV have a better ability to separate electron–hole pairs [51]. In addition, it also confirms that 1.0% Au/BYV has the best performance for charge separation, thus possessing the highest photocatalytic activity. Fig. 25c shows the examination of linear sweep voltammetry (LSV) by investigating the overpotential of CO evolution. The corresponding Tafel plot was shown in Fig. 25d. It illustrates the overpotentials of BYV, 1.0% Au/BYV are 0.38 V, 0.28 V, respectively. Clearly, compared

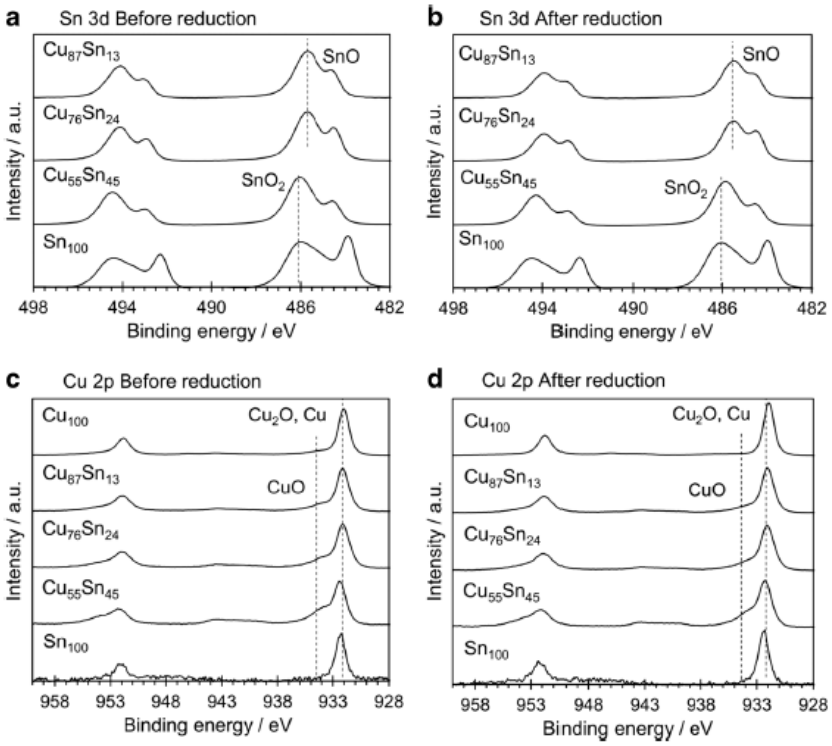

Figure 21: XPS spectra. **a** Sn 3d spectra of $Cu_{87}Sn_{13}$, $Cu_{76}Sn_{24}$, $Cu_{55}Sn_{45}$, and Sn before reduction. **b** Sn 3d spectra after reduction. **c** Cu 2p spectra Cu_{100}, $Cu_{87}Sn_{13}$, $Cu_{76}Sn_{24}$, $Cu_{55}Sn_{45}$, and Sn before reduction. **d** Cu 2p spectra after reduction. The broken line indicates the position of each chemical bonding state: SnO_2, SnO, CuO, Cu_2O, and Cu. Adapted from Electrocatalysis, Springer. DOI: 10.1007/s12678-017-0434-2

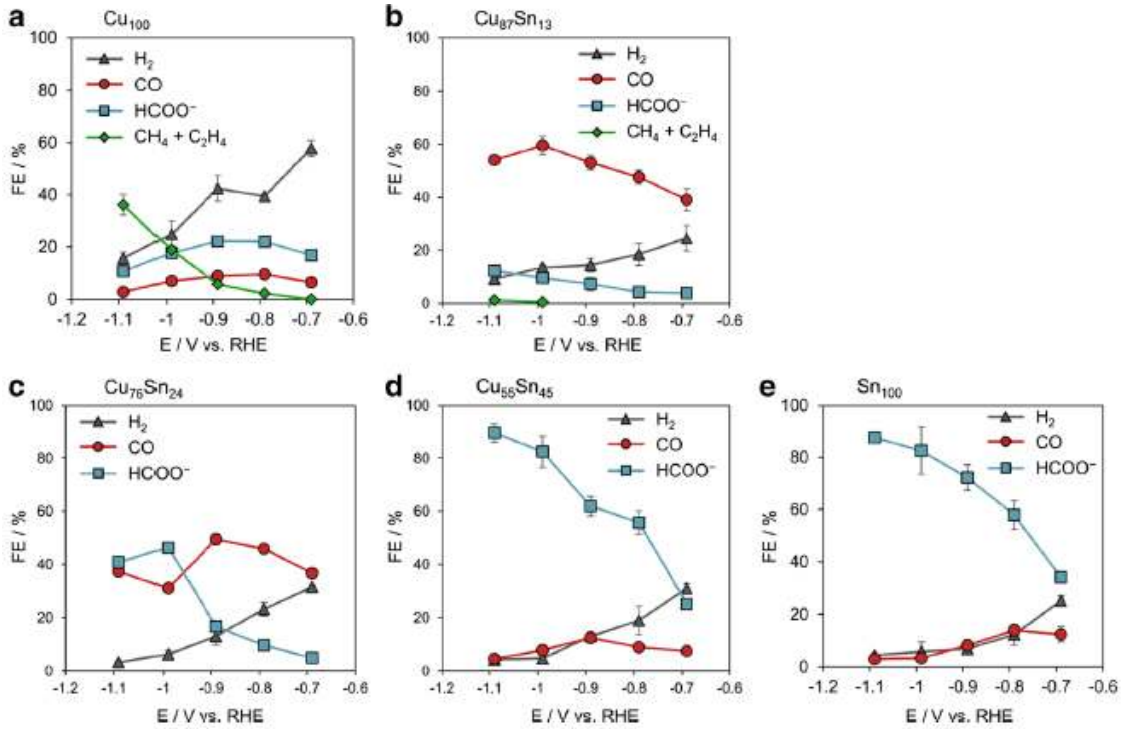

Figure 22: Faradaic efficiency of CO_2 electroreduction products as a function of potential. **a** Cu_{100}; **b** $Cu_{87}Sn_{13}$; **c** $Cu_{76}Sn_{24}$; **d** $Cu_{55}Sn_{45}$; **e** Sn_{100} deposited on Cu plate. Electrolyte, 0.1 M $KHCO_3$. Adapted from Electrocatalysis, Springer. DOI: 10.1007/s12678-017-0434-2

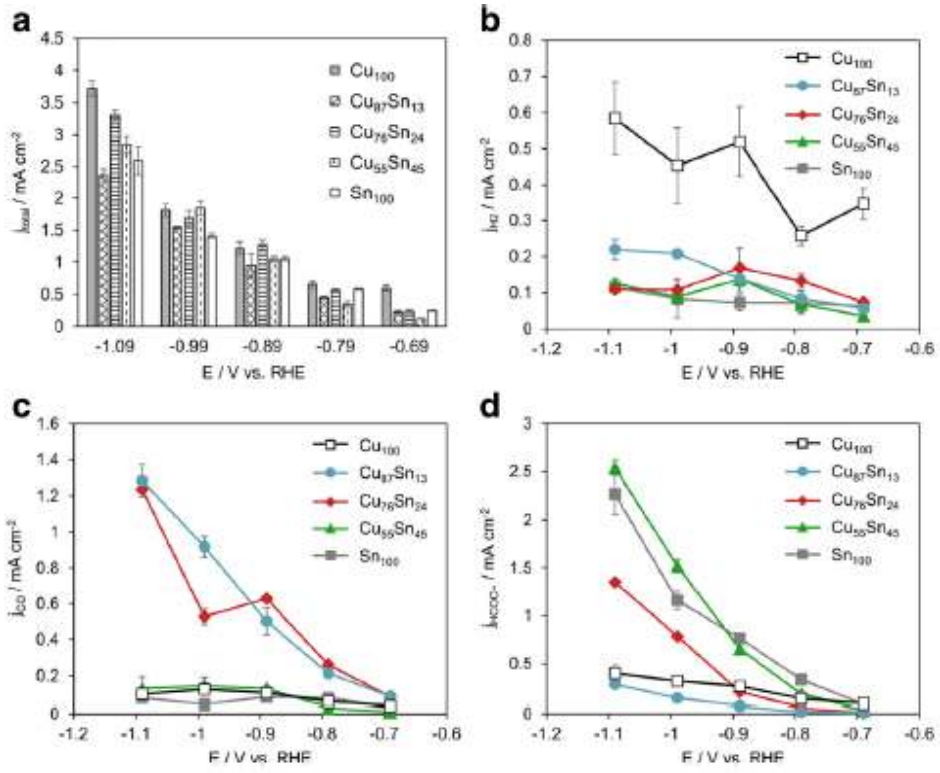

Figure 23: Total current density for CO_2 electroreduction as a function of potential on Cu_{100}, $Cu_{87}Sn_{13}$, $Cu_{76}Sn_{24}$, $Cu_{55}Sn_{45}$, and Sn_{100}. **a** Partial current density of the products from CO_2 reduction on each catalyst: **b** H_2; **c** CO; **d** $HCOO^-$. Adapted from Electrocatalysis, Springer. DOI: 10.1007/s12678-017-0434-2

Table 2: Electrodeposition condition of various catalysts. The composition ratio of each Cu-Sn alloy was decided by AES analysis. Adapted from Electrocatalysis, Springer. DOI: 10.1007/s12678-017-0434-2

	Cu	$Cu_{87}Sn_{13}$	$Cu_{76}Sn_{24}$	$Cu_{55}Sn_{45}$	Sn
$K_4P_2O_7$ (M)	0.5	0.5	0.5	0.5	0.5
$C_6H_{14}N_2O_7$ (M)		0.05	0.05		
$C_4H_{12}N_2O_5$ (M)	0.2				
$CuSO_4.5H_2O$ (M)	0.2	0.18	0.16	0.1	
$SnSO_4$ (M)		0.02	0.04	0.1	0.2
PEG 6000 (g/L)					1
Formalin (mL/L)					0.6
Current density (mA/cm^2)	5.6	3.2	3.2	3.6	1
Deposition time (min)	5	5	5	5	5

with pure BYV, the lower overpotential was gained after Au loading, which is vital for CO evolution.

Zeng et al reported the fabrication of heterogeneous-phase solid-solution $Zn_XCa_{1-X}In_2S_4$ between trigonal $ZnIn_2S_4$ and cubic $CaIn_2S_4$ [52]. In their achievement, they found that the $Zn_XCa_{1-X}In_2S_4$ solid solutions with orderly tuned photoresponsive range from 540nm to 640nm all have more negative conduction band (CB) level and highly enhanced charge separation efficiency. Finally, they suggested that their work may provide new perspective into development of a efficient, visible-light driven photocatalyst for CO_2 reduction and other photo-reduction reaction.

The photocatalytic overall conversion of CO_2 with H_2O to chemical fuel and oxygen mimicking natural

Table 3: Relative composition ratios on the surfaces of the prepared catalysts, as per AES measurements. Adapted from Electrocatalysis, Springer. DOI: 10.1007/s12678-017-0434-2

	Relative composition ratio (%)									Cu%
	Cu	Sn	C	O	Si	K	P	N	S	
Sn100	2.2	30.0	4.4	42.5	-	18.5	2.4	-	-	
Sn100-AR[a]	5.8	44.4	10.7	39.1	-	-	-	-	-	
Cu55Sn45	25.2	20.8	14.1	37.4	2.5	-	-	-	-	55
Cu55Sn45-AR[a]	29.2	21.8	13.0	34.0	2.0	-	-	-	-	57
Cu76Sn24	41.3	12.9	14.6	31.2	-	-	-	-	-	76
Cu76Sn24-AR[a]	43.7	10.0	19.6	26.7	-	-	-	-	-	81
Cu87Sn13	50.3	7.3	15.0	27.4	-	-	-	-	-	87
Cu87Sn13-AR[a]	48.0	6.1	21.4	24.5	-	-	-	-	-	89
Cu100		49.8	-	22.6	21.1	-	-	-	4.9	1.6
Cu100-AR[a]	44.9	-	25.8	18.2	-	-	-	10.1	1.1	

[a] After CO_2 reduction in 0.1 M $KHCO_3$ at – 0.89 V vs RHE

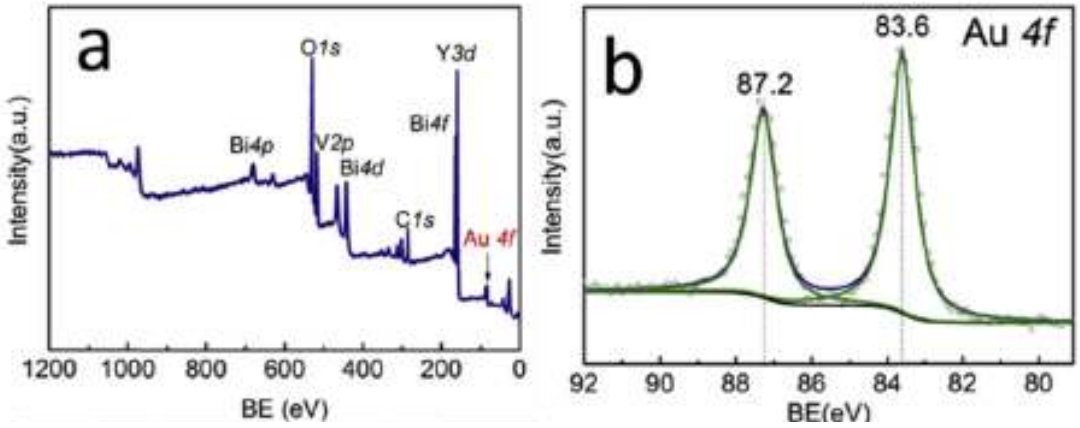

Figure 24: XPS survey spectrum of 1.0 wt% Au/BYV (a) and HR-XPS spectra of Au cocatalyst (b); TEM images. Adapted from Materials Letters, Elsevier. DOI 10.1016/j.matlet.2018.11.150

photosynthesis is a huge challenge in photocatalysis. Gao et al. worked on Persian buttercup-like $BiOBr_xCl_{1-x}$ solid solution and achieved photocatalytic overall CO_2 reduction to CO and O_2 [53].

7 Conclusion

Solid solutions have been shown greatly as a support and also as electrocatalysts and photocatalyst, with outstanding performances. There were great achievements in stability, selectivity, efficiency and overpotential in the electrocatalysts and photocatalysts reported. XPS data has shown satisfactory results in the area of oxygen reduction reaction, oxygen evolution reaction, hydrogen evolution reaction, overall water splitting and carbon dioxide reduction reaction. This includes a record low overpotential of 178mV at $10mAcm^{-2}$ and maintenance of excellent performance throughout the 10h chronopotentiometry test at a constant current of $10mAcm^{-2}$ in 0.5M H_2SO_4 solution. Preparation of Cu-Sn alloy catalytic electrodes was achieved through the simple electrodeposition method for electrochemical CO_2 reduction. A small-sized amorphous Fe-Ni-Ox NPs approximately 20 nm in size possessing more

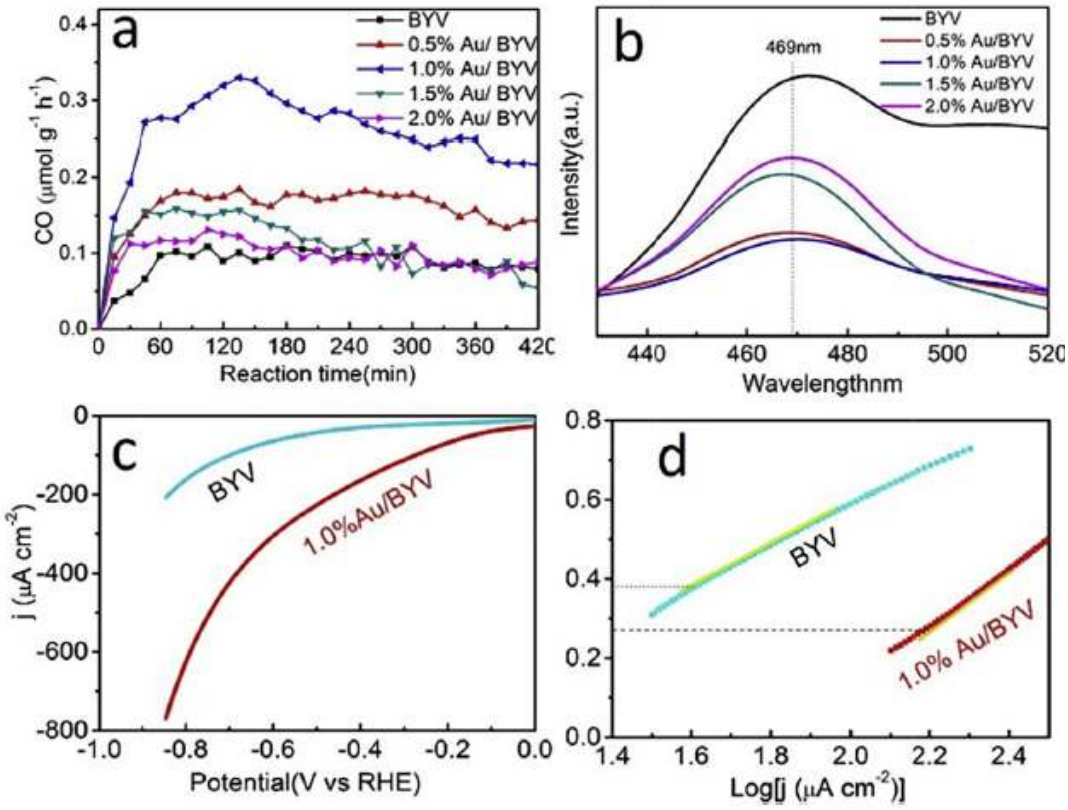

Figure 25: CO evolution rates (a) and PL spectra (b) of BYV with different Au loading contents; LSV curves of BYV and 1.0 wt% Au/BYV samples (c) and the corresponding Tafel plots (d) in 0.1 M $KHCO_3$ aqueous solution with saturated CO_2. Adapted from Materials Letters, Elsevier. DOI 10.1016/j.matlet.2018.11.150

active sites and higher active surface areas with an aerosol spray-assisted approach was prepared using iron/nickel acetylacetonates as the raw materials instead of inorganic salts. Investigation of the electrocatalytic performance of $Mo_x W_{1-x} S_2$ ($0 \leq x \leq 1$) systems grown from 3D freestanding interconnected glassy carbon foam to form a platform with different ratios of Mo and W in the $Mo_x W_{1-x} S_2$ solid solution was performed. Successful preparation of $Cu_{0.8}Ga_{0.4}In_{0.4}Zn_{0.4}S_2$ (x=0.2, y=0.5) photocatalyst powder as a micrometer-sized single phase crystal by a flux method using LiCl-KCl molten salt was shown. Successful design and synthesis of Ni/Co nitrides ($Ni_xCo_{3-x}N$) solid-solutions decorated on nitrogen doped carbon nanotubes (NCNT) as highly stable bi-functional ORR and OER electrocatalysts for Zn-air batteries was achieved. The NCNTs provided a conductive and porous framework for fast ion and electron dissusion to enhance mass-transport, and one-step approach to improve the HER activity of MoS_2 and MoP via formation of a $MoS_{2(1-x)}P_x$ ($x = 0$ to 1) solid solution.

References

[1] Li, Rengui, and Can Li. "Photocatalytic water splitting on semiconductor-based photocatalysts." *Advances in catalysis*. Vol. 60. Academic Press, 2017. 1-57.

[2] Foster, Shelby L., et al. "Catalysts for nitrogen reduction to ammonia." *Nature Catalysis* 1.7 (2018): 490.

[3] Cai, Zhixiong, et al. "Nanomaterials With Different Dimensions for Electrocatalysis." *Novel Nanomaterials for Biomedical, Environmental and Energy Applications*. Elsevier, 2019. 435-464.

[4] Löffler, Tobias, et al. "Toward a Paradigm Shift in Electrocatalysis Using Complex Solid Solution Nanoparticles." *ACS Energy Letters* 4.5 (2019): 1206-1214.

[5] Kibsgaard, Jakob, and Ib Chorkendorff. "Considerations for the scaling-up of water splitting catalysts." *Nature Energy* (2019): 1.

[6] *Z.W. Seh et al., Science, 2017*

[7] Shi, Meiqin, et al. "Enhanced Electrocatalytic Oxygen Reduction on NiWO x Solid Solution with Induced Oxygen Defects." *ACS applied materials & interfaces* 9.40 (2017): 34990-35000.

[8] Huang, J. H.; Chen, J. T.; Yao, T.; He, J. F.; Jiang, S.; Sun, Z. H.; Liu, Q. H.; Cheng, W. R.; Hu, F. C.; Jiang, Y. et al. CoOOH Nanosheets with high mass activity for water oxidation. Angew. Chem., Int. Ed. 2015, 54, 8722–8727.
[9] Wang, Lingxiao, et al. "Facile synthesis of Fe/Ni bimetallic oxide solid-solution nanoparticles with superior electrocatalytic activity for oxygen evolution reaction." *Nano research* 8.12 (2015): 3815-3822.
[10] Yu, X. W.; Zhang, M.; Yuan, W. J.; Shi, G. Q. A highperformance three-dimensional Ni–Fe layered double hydroxide/graphene electrode for water oxidation. J. Mater. Chem. A 2015, 3, 6921–6928.
[11] Kim, J. et al. High-performance pyrochlore-type yttrium ruthenate electrocatalyst for oxygen evolution reaction in acidic media. J. Am. Chem. Soc. 139, 12076–12083 (2017).
[12] Morgan, D. J. Resolving ruthenium: XPS studies of common ruthenium materials. Surf. Interface Anal. 47, 1072–1079 (2015).
[13] Guan, B. Y., Yu, L. & Lou, X. W. General synthesis of multishell mixed-metal oxyphosphide particles with enhanced electrocatalytic activity in the oxygen evolution reaction. Angew. Chem. Int. Ed. 56, 2386–2389 (2017).
[14] Lin, Yichao, et al. "Chromium-ruthenium oxide solid solution electrocatalyst for highly efficient oxygen evolution reaction in acidic media." *Nature communications* 10.1 (2019): 162.
[15] Seh, Z. W. et al. Combining theory and experiment in electrocatalysis: Insights into materials design. Science 355, eaad4998 (2017).
[16] Liu, J., Zhu, D., Guo, C., Vasileff, A. & Qiao, S.-Z. Design strategies toward advanced MOF-derived electrocatalysts for energy-conversion reactions. Adv. Energy Mater. 7, 1700518 (2017).
[17] Mao, L. Q. et al. The role of temperature on Cr(VI) formation and reduction during heating of chromium-containing sludge in the presence of CaO. Chemosphere 138, 197–204 (2015).
[18] McCrory, C. C. L. et al. Benchmarking hydrogen evolving reaction and oxygen evolving reaction electrocatalysts for solar water splitting devices. J. Am. Chem. Soc. 137, 4347–4357 (2015).
[19] Kibis, Lidiya S., et al. "Redox and Catalytic Properties of Rh x Ce1–x O2– δ Solid Solution." *The Journal of Physical Chemistry C* 121.48 (2017): 26925-26938.
[20] Wang, Lu, et al. "$MoxW_{1-x}S_2$ solid solutions as 3D electrodes for hydrogen evolution reaction." *Advanced Materials Interfaces* 2.9 (2015): 1500041.
[21] T. Wilberforce, Z. E. Hassan, F. N. Khatib, A. A. Makky, A. Baroutaji, J. G. Carton, A. G. Olabi, Int. J. Hydrogen Energy, 42 (2017) 25695.
[22] D. Gao, J. N. Guo, X. Cui, L. Yang, Y. Yang, H. C. He, P. Xiao, Y. H. Zhang, ACS Appl. Mater. Interfaces, 9 (2017) 22420.
[23] Yang, Yufang, et al. "Synthesis and characterization of Ni-Co electrocatalyst for hydrogen evolution reaction in acidic media." *Int J Electrochem Sci* 13.7 (2018): 7193-7205.
[24] Ye, Ruquan, et al. "High-Performance Hydrogen Evolution from MoS2 (1–x) P x Solid Solution." *Advanced Materials* 28.7 (2016): 1427-1432.
[25] Geng, J.; Kuai, L.; Kan, E. J.; Wang, Q.; Geng, B. Y. Preciousmetal-free Co-Fe-O/rGO synergetic electrocatalysts for oxygen evolution reaction by a facile hydrothermal route. ChemSusChem 2015, 8, 659–664.
[26] Oxygen Reduction in Alkaline Media: From Mechanisms to Recent Advances of Catalysts
[27] Zhao, Yige, et al. "Pt–Co secondary solid solution nanocrystals supported on carbon as next-generation catalysts for the oxygen reduction reaction." *Journal of Materials Chemistry A* 3.40 (2015): 20086-20091.
[28] Shi, Meiqin, et al. "Enhanced Electrocatalytic Oxygen Reduction on NiWO x Solid Solution with Induced Oxygen Defects." *ACS applied materials & interfaces* 9.40 (2017): 34990-35000.
[29] Ghadge, Shrinath Dattatray, et al. "Fluorine substituted (Mn, Ir) O 2: F high performance solid solution oxygen evolution reaction electro-catalysts for PEM water electrolysis." *RSC Advances* 7.28 (2017): 17311-17324.
[30] He, Guanjie, et al. "Solid solution nitride/carbon nanotube hybrids enhance electrocatalysis of oxygen in zinc-air batteries." *Energy Storage Materials* 15 (2018): 380-387.
[31] C. Tang, B. Wang, H.F. Wang, Q. Zhang, Defect engineering toward atomic Co-Nx-C in hierarchical graphene for rechargeable flexible solid Zn-air batteries, Adv. Mater. 29 (2017) 1703185.
[32] G.-L. Chai, K. Qiu, M. Qiao, M.-M. Titirici, C. Shang, Z.X. Guo, Active sites engineering leads to exceptional ORR and OER bifunctionality in P, N Co-doped graphene frameworks, Energy Environ. Sci. 10 (2017) 1186–1195.
[33] S. Dou, L. Tao, J. Huo, S. Wang, L. Dai, Etched and doped Co9S8/graphene hybrid for oxygen electrocatalysis, Energy Environ. Sci. 9 (2016) 1320–1326.
[34] C. Hu, L. Dai, Multifunctional carbon-based metal-free electrocatalysts for simultaneous oxygen reduction, oxygen evolution, and hydrogen evolution, Adv. Mater. 29 (2017) 1604942
[35] Y. Yu, W. Gao, Z. Shen, Q. Zheng, H. Wu, X. Wang, W. Song, K. Ding, A novel Ni3N/ graphene nanocomposite as supercapacitor electrode material with high capacitance and energy density, J. Mater. Chem. A 3 (2015) 16633–16641.
[36] Chen, T.-Y. et al. Heterojunction confinement on the atomic structure evolution of near monolayer core–shell nanocatalysts in redox reactions of a direct methanol fuel cell. J. Mater. Chem. A 3, 1518–1529 (2015).
[37] Jayaramulu, Kolleboyina, et al. "Nanoporous Nitrogen-Doped Graphene Oxide/Nickel Sulfide Composite Sheets Derived from a Metal-Organic Framework as an Efficient Electrocatalyst for Hydrogen and Oxygen Evolution." *Advanced Functional Materials* 27.33 (2017): 1700451.
[38] Tan, Chaoliang, et al. "Recent advances in ultrathin two-dimensional nanomaterials." *Chemical reviews* 117.9 (2017): 6225-6331.
[39] Bhadram, Venkata S., et al. "Zn x Mn1–x O Solid Solutions in the Rocksalt Structure: Optical, Charge Transport, and Photoelectrochemical Properties." *ACS Applied Energy Materials* 1.2 (2018): 260-266.
[40] Lardhi, Sheikha, et al. "Ab initio assessment of Bi 1– x RE x CuOS (RE= La, Gd, Y, Lu) solid solutions as a semiconductor for photochemical water splitting." *Physical Chemistry Chemical Physics* 19.19 (2017): 12321-12330.
[41] Wan, Meng, et al. "Nitrogen anion-decorated cobalt tungsten disulfides solid solutions on the carbon nanofibers for water splitting." *Nanotechnology* 29.38 (2018): 385602.

[42] Velický, Matěj, and Peter S. Toth. "From two-dimensional materials to their heterostructures: An electrochemist's perspective." *Applied Materials Today* 8 (2017): 68-103.
[43] Sivanantham, Arumugam, Pandian Ganesan, and Sangaraju Shanmugam. "Hierarchical NiCo2S4 nanowire arrays supported on Ni foam: an efficient and durable bifunctional electrocatalyst for oxygen and hydrogen evolution reactions." *Advanced Functional Materials* 26.26 (2016): 4661-4672.
[44] Chen, Shanshan, Tsuyoshi Takata, and Kazunari Domen. "Particulate photocatalysts for overall water splitting." *Nature Reviews Materials* 2.10 (2017): 17050.
[45] Xiao, Changlong, et al. "Nanostructured gold/bismutite hybrid heterocatalysts for plasmon-enhanced photosynthesis of ammonia." *ACS Sustainable Chemistry & Engineering* 5.11 (2017): 10858-10863.
[46] Chen, Wei, et al. "Non-noble metal Cu as a cocatalyst on TiO2 nanorod for highly efficient photocatalytic hydrogen production." *Applied Surface Science* 445 (2018): 527-534.
[47] Geng, J.; Kuai, L.; Kan, E. J.; Wang, Q.; Geng, B. Y. Preciousmetal-free Co-Fe-O/rGO synergetic electrocatalysts for oxygen evolution reaction by a facile hydrothermal route. ChemSusChem 2015, 8, 659–664.
[48] Hayashi, Toshio, et al. "Powder-based (CuGa 1– y In y) 1– x Zn 2x S 2 solid solution photocathodes with a largely positive onset potential for solar water splitting." *Sustainable Energy & Fuels* 2.9 (2018): 2016-2024.
[49] Chen, Wei, Yanhong Wang, and Wenfeng Shangguan. "Au as a cocatalyst loaded on solid solution Bi0. 5Y0. 5VO4 for enhancing photocatalytic CO_2 reduction activity." *Materials Letters* 238 (2019): 74-76.
[50] Chen, Wei, Yanhong Wang, and Wenfeng Shangguan. "Au as a cocatalyst loaded on solid solution Bi0. 5Y0. 5VO4 for enhancing photocatalytic CO_2 reduction activity." *Materials Letters* 238 (2019): 74-76.
[51] Chen, W.; Wang, H. T.; Li, Y. Z.; Liu, Y. Y.; Sun, J.; Lee, S. H.; Lee, J.-S.; Cui, Y. In situ electrochemical oxidation tuning of transition metal disulfides to oxides for enhanced water oxidation. ACS Cent. Sci. 2015, 1, 244–251.
[52] Zeng, Chao, et al. "Fabrication of Heterogeneous-Phase Solid-Solution Promoting Band Structure and Charge Separation for Enhancing Photocatalytic CO2 Reduction: A Case of $Zn_x Ca_{1-x} In_2S_4$." *ACS applied materials & interfaces* 9.33 (2017): 27773-27783.
[53] Gao, Meichao, et al. "Persian buttercup-like $BiOBr_xCl_{1-x}$ solid solution for photocatalytic overall CO_2 reduction to CO and O_2." *Applied Catalysis B: Environmental* 243 (2019): 734-740.